A Continuum from Halogen Bonds to Covalent Bonds: Where Do λ^3 Iodanes Fit?

Seth Yannacone [1], **Vytor Oliveira** [2], **Niraj Verma** [1] and **Elfi Kraka** [1,*]

[1]   Department of Chemistry, Southern Methodist University, 3215 Daniel Avenue, Dallas, TX 75275-0314, USA;
      syannacone@smu.edu (S.Y.); nirajv@smu.edu (N.V.)
[2]   Instituto Tecnológico de Aeronáutica (ITA), Departamento de Química, São José dos Campos,
      12228-900 São Paulo, Brazil; vytor3@gmail.com
*   Correspondence: ekraka@smu.edu; Tel.: +1-214-768-2611

Abstract: The intrinsic bonding nature of λ^3-iodanes was investigated to determine where its hypervalent bonds fit along the spectrum between halogen bonding and covalent bonding. Density functional theory with an augmented Dunning valence triple zeta basis set (ωB97X-D/aug-cc-pVTZ) coupled with vibrational spectroscopy was utilized to study a diverse set of 34 hypervalent iodine compounds. This level of theory was rationalized by comparing computational and experimental data for a small set of closely-related and well-studied iodine molecules and by a comparison with CCSD(T)/aug-cc-pVTZ results for a subset of the investigated iodine compounds. Axial bonds in λ^3-iodanes fit between the three-center four-electron bond, as observed for the trihalide species IF_2^- and the covalent FI molecule. The equatorial bonds in λ^3-iodanes are of a covalent nature. We explored how the equatorial ligand and axial substituents affect the chemical properties of λ^3-iodanes by analyzing natural bond orbital charges, local vibrational modes, the covalent/electrostatic character, and the three-center four-electron bonding character. In summary, our results show for the first time that there is a smooth transition between halogen bonding $\rightarrow$ 3c–4e bonding in trihalides $\rightarrow$ 3c–4e bonding in hypervalent iodine compounds $\rightarrow$ covalent bonding, opening a manifold of new avenues for the design of hypervalent iodine compounds with specific properties.

1. Introduction

Hypervalent iodine compounds (HVI) are important alternatives to transition metal reagents because of their reactivity, synthetic utility, low cost, abundance, and non-toxic nature [1–6]. HVIs are involved in a multitude of reactions such as: reductive elimination, ligand exchange, oxidative addition, and ligand coupling [7,8]. The three-center four-electron bonds (3c–4e) in HVI are weak and polarizable, which is valuable in synthetic organic chemistry, as they can exchange leaving groups or accept electrophilic/nucleophilic ligands depending on their surroundings [9]. Despite such utility, there are still unknowns regarding the intrinsic bonding nature of HVIs and hypervalency in general. Though iodine is a halogen, it behaves like a metal; it is the heaviest non-radioactive element of the periodic table and is the most polarizable halogen [10,11]. Because of its diffuse electron density (van der Waals (vdW) radius of ca 2 Å), iodine is a good electron donor, but can also serve as an electron acceptor [12,13]. Iodine is not known to participate in d-orbital or π-interactions, though this could be further investigated [14,15].

HVIs commonly exist in the oxidation states 3, 5, and 7, which support 10, 12, and 14 valence electrons, respectively [16]. Most common are the oxidation states 3 and 5, which are referred to as

λ^3 and λ^5-iodanes [17]. λ^3-iodanes form distorted T-shaped molecular geometries, while λ^5-iodanes generally prefer square pyramidal geometries, as confirmed through both X-ray crystallography and computational studies [18,19]. These somewhat unusual molecular geometries are the result of the pseudo-Jahn–Teller effect [20]. The atoms that make up the "T" in λ^3-iodanes form improper dihedrals and non-ideal bond angles. The causes of these angular and dihedral deviations are unknown, but have been related to the anisotropic nature of the electronic density distribution in iodine [21–25]. Bader et al. showed that the vdW radius in iodine is larger at the equatorial position than at the axial position [26–28]. This supports the observation that electronegative ligands favor the axial positions in iodine [29].

Hypervalency has been defined in several ways: Musher characterized main group elements in higher oxidation states as hypervalent [30]. A successful concept employed to explain hypervalency without involving d-orbitals is the formation of multi-centered electron-deficient bonds [31–33]. In this context, the 3c–4e bond model of Pimentel–Rundle is especially useful. According to this model, three atoms linearly align, each of which contributes an atomic orbital to form three molecular orbitals; a bonding orbital, a non-bonding orbital, and an antibonding orbital. Since only four electrons are involved, the antibonding orbital is unoccupied. As a result, two bonds share a single bonding electron pair (i.e., they have a fractional bond order of 0.5). The formation of two or more electron-deficient bonds allows hypervalent compounds to have higher oxidation states without necessarily expanding their octets. A direct consequence of this model is that the 3c–4e bond is expected to be substantially weaker than the two-center two-electron (2c–2e) bond in a given hypervalent molecule. Even though there are various works showing that d-orbital contributions to hypervalent bonds (HVB) are minimal, many chemistry text books still make use of the idea of an extended octet and the formation of spd-hybrid orbitals to explain HVB [34]. There is a strong overlap between the concepts of fractional bond order, the 3c–4e bond, and the halogen bond (XB) in trihalides, which are considered prime examples of 3c–4e bonding, but also strong XB [35,36]. A formal definition of XB is given in the following paragraph.

3c–4e HVI bonding (3c–4e HVIB) draws comparisons to the secondary bonding interaction due to the weak bond strength, high reactivity, and long internuclear distances exceeding covalent bond lengths [37]. 3c–4e HVIB also shares similarities with non-covalent interactions, along with hydrogen bonding [38–40], XB [35,41–43], pnicogen bonding [43–45], chalcogen bonding [43,46], and tetrel bonding [47]. XB is a non-covalent interaction between an electrophilic halogen (X) and a nucleophile with a lone pair (lp(A)) of donating electrons [42,43]. For the remainder of this work, we will express lone pairs as (lp).The nucleophile/halogen acceptor (A), donates electrons to the antibonding (σ*(XY)) orbital of the halogen donor (Y) [48,49]. XB is also known to have an X–A distance that is shorter than the sum of the vdW radii with Y–X–A angles close to 180 degrees [35,41,50,51]. Because of the obvious similarities between 3c–4e HVIB and XB, it has been argued that HVB should not be considered as a special bonding class [52,53]. On the other hand, the term hypervalency has been widely accepted by the chemistry community, and therefore, its continuous use has been advocated [54]. Based on this controversy, we decided to delve deeper into the bonding nature of λ^3-iodanes.

In this work, we investigated the intrinsic nature of HVIB in λ^3-iodanes and its relation to XB, 3c–4e bonding in trihalides, and covalent bonding to determine if there is a smooth transition between these interactions. Additionally, we studied the role equatorial ligands play in strengthening the 3c–4e bond in λ^3-iodanes, as well as substituent effects in the axial ligands. We utilized density functional theory (DFT), vibrational spectroscopy, quantum theory of atoms in molecules (QTAIM) combined with the Cremer–Kraka criterion for covalent bonding [55–57], and the natural bond orbital (NBO) analysis to characterize the nature and the intrinsic strength of HVIB. This investigation was rationalized by studying a diverse group of 34 HVI compounds shown in Figure 1, including known chemical compounds complemented by some model compounds. The remainder of this work is presented as follows: data, results, and discussion are presented in Section 2; Section 3 gives a description of the computational methods utilized; and Section 4 gives conclusions, the outlook, and future goals.

2. Results and Discussion

Figure 1 shows the 34 HVI compounds with selected NBO charges investigated in this work. Note that the abbreviation (PhI) is used to refer to iodobenzenes.
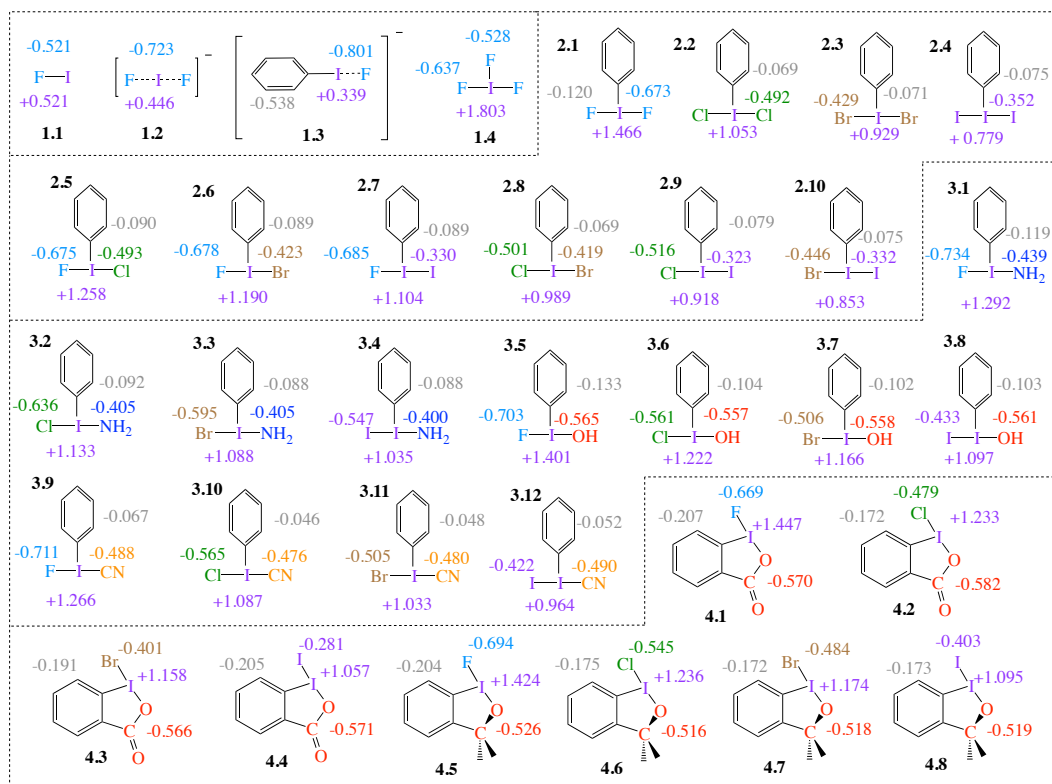

Figure 1. Schematic of the 34 molecules investigated showing the numbering system (group.molecule, e.g., **1.1–4.8**) given in bold face, and natural bond orbital (NBO) charges calculated at the ωB97X-D/aug-cc-pVTZ level of theory. Note: charges in grey, blue, red, and orange are Ph/benzene, NH_2, OH, OCO (red), OC$(CH_3)_2$ (red), and CN group charges, respectively, and not atomic charges.

The compounds are organized into four groups. **Group 1** contains four reference compounds; the covalent complex FI (**1.1**), the 3c–4e trihalide IF_2^- (**1.2**), fluorophenyl iodide (**1.3**), and the λ^3-iodane, IF_3 (**1.4**), which is used to study the effects of electronegative equatorial ligands. **Group 2** and **Group 3** compounds, iodobenzenes (**2.1–2.10**) and (**3.1–3.11**), respectively, represent λ^3-iodanes with a phenyl group equatorially bound to I. While both axial ligands in **Group 2** molecules are halogen atoms, in **Group 3**, the axial ligands consist of a halogen and a non-halogen lone-pair-bearing functional group (CN, NH_2, and OH). **Group 4** consists of four halobenziodazoles (**4.1–4.4**) and four halobenziodoxoles (**4.5–4.8**).

2.1. NBO Charge Analysis

XB is a non-covalent interaction formed between a halogen donor molecule (YX) (e.g., a dihalogen, interhalogen, or halogenated molecule) and a halogen acceptor atom A, where A is an electron-rich atom; e.g., a nucleophilic heteroatom with lone-pair (lp) electrons [9,35,41–43]. The general charge transfer picture in XB describes a transfer of charge from lp (A) into the empty σ^*(YX) orbital [36,58,59]. Applied to our set of HVI compounds, there are two possibilities to define the YI and the IA part of **Group 2** molecules **2.5–2.10**. In these cases, we chose IA to be the weaker of the two axial bonds, in analogy to XB. The same definition was also applied for **Group 3** and **Group 4** compounds.

For all 34 HVI compounds investigated in this work, the central iodine atom I holds a positive charge (see purple numbers in Figure 1), ranging from +0.339 e in **1.3** to +1.803 e in **1.4**. There is a significant difference in the central iodine charge when comparing the λ^3-iodanes with the three reference compounds **1.1–1.3** for which the iodine charge ranges from +0.339 e to +0.521 e, whereas iodine charges in λ^3-iodanes range from +0.779 e in **2.4** to +1.803 e in **1.4**. The obvious difference between the λ^3 HVIs and the non-HVIs is the equatorial ligand, which is absent in **1.1–1.3**. In every case, except **1.4**, the equatorial ligand is a phenyl (Ph) group (**Groups 2–3**) or a benzene ring (**Group 4**). Group charges for Ph/benzene ligands are negative in every case, as are charges on the Ph/benzene C atom bound to I, as shown in Figure 1. Increased positive charge on I indicates that the equatorial ligands are pulling charge from the central I. In **1.4**, the equatorial ligand is F; this is an extreme case of a strong electron-withdrawing ligand in the equatorial position, which polarizes the central I atom. As a result, each I–F interaction involved in the 3c–4e bond becomes more polar.

2.1–2.4 comprise λ^3-iodanes of the type PhIA$_2$, for A = F, Cl, Br, and I. Caused by the increasing electronegativity from I to F, the bond polarity increases from I–I < Br–I < Cl–I < F–I, with the positive charge on the central I atom increasing in the same order, i.e., +0.779 e in **2.4** to +1.466 e in **2.1**. The same trend is observed in **2.5–2.7**. As the second substituent changes from Cl to I, charge on the F ligand remains almost unchanged ($\Delta q = -0.012$ e), while the positive charge on I decreases. The same pattern continues for compounds **2.8–2.10**. The charge on the equatorial ligand appears to be independent of the axial ligands for **Group 2**, with the exception of **2.1**, **2.5–2.7** with F as the common axial ligand. The charge on the equatorial ligand in these cases tends to be most negative (ranging between −0.089 e and −0.120 e) compared to the other **Group 2** members (ranging between −0.069 e and −0.079 e).

In **Group 3**, one of the axial halogen atoms is replaced with a functional group (NH$_2$, OH, and CN). For comparison, we refer to OCO and OC(CH$_3$) in the halobenziodazoles **4.1–4.4** and halobenziodoxoles **4.5–4.8** of **Group 4** as functional groups; see Figure 1. In **3.2–3.4**, charge on NH$_2$ remains consistent. **3.1** is the exception, but the charge difference between these four molecules is −0.034 e. This trend is observed in **3.5–4.8** as well, where Δq (OH) = −0.008 e, Δq (OCO) = −0.016 e, Δq (OC(CH$_3$)$_2$) = −0.007 e, and Δq (CN) = −0.014 e. An important trend is revealed: although the charge at the central I atom is dependent on both axial ligands, charge on the functional group is insensitive to the halogen substituents at the opposite side, particularly for Cl, Br, and I. The behavior of the axial halogens in **Group 3** is the same as described for **Group 2**. The functional group with the largest net negative charge is the OCO group, followed by OH, OC(CH$_3$)$_2$, CN, and NH$_2$, respectively. The data reveal yet another important trend: the more electronegative the axial ligands are, the more negative charge they collect and the more negative charge they impose on the equatorial ligand. Considering the charge on the Ph group for **Group 3** and the benzene ring for **Group 4**, almost the same functional group trend emerges: there is an increase of negative charge from NH$_2$ < CN < OH < OC(CH$_3$)$_2$ < OCO, with OH and OC(CH$_3$)$_2$ groups being interconverted. That means, regarding the equatorial ligands, the same trends are observed in **Group 2** molecules and in **Groups 3–4** molecules. For all compounds with an axial F atom, charge on the equatorial ligand becomes more negative. The benzene rings of **Group 4** molecules have a substantial negative charge ranging from −0.172 e to −0.207 e, however less than the Ph group of **1.3**, being −0.538 e.

2.2. Bond Strength Order

Interatomic distances (r), $\rho(\mathbf{r}_b)$, $H(\mathbf{r}_b)$, k^a, BSO n values, and local mode frequencies (ω^a) are summarized in Tables 1 and 2. Figures 2–4 show the power relationship between BSO n and k^a for **Group 1**, Y$\cdots$IA and YI$\cdots$A in **Groups 2–4**, where YI$\cdots$A is weaker than Y$\cdots$IA, and I–C equatorial (Ph, F, benzene) bonds in **Groups 1–4**. Note: in Table 1, the F$\cdots$I interactions in **3.9** and **4.1** are the stronger bonds. These are the only two cases in **Groups 3–4** where the halogen$\cdots$I interaction is the stronger interaction. Therefore, CN and OCO will be considered A and F will be considered Y in Table 1 for these two cases only. However, this convention is not used for the BSO n plots in Figures 3 and 5. In these two figures, the Y$\cdots$IA interaction is the bond between the non-halogen and I, and YI$\cdots$A is

the bond between the halogen and I. Figure 2a is a BSO *n* plot for interactions in **1.1–2.1**. Comparing bond strength in axial I–F interactions in FI, IF_3, $PhIF_2$, IF_2^-, and $PhIF^-$ reveals the hypothesized trend: $FI > IF_3$ (3c–4e HVIB) $> PhIF_2$ (3c–4e HVIB) $> IF_2^-$ (3c–4e) $> PhIF^-$ (XB). As expected, the 2c–2e FI bonds in **1.1** and **1.4** are stronger than 3c–4e in **1.2** and **1.4**. The latter are stronger than the I$\cdots$F XB in **1.3**, as shown in Table 1 and Figure 2. It is notable that the hypervalent IF_3 forms a shorter and stronger 2c–2e bond compared to the FI molecule. Axial F atoms pull charge from iodine, resulting in a more polar 2c–2e I–F bond, and also contract the I orbital, improving I–F orbital overlap. The 3c–4e bond in IF_3 is stronger than that of $PhIF_2$ because the equatorial F polarizes the central I, causing more polar and stronger interactions at the axial positions. The equatorial Ph and benzene groups do not have the polarizing ability of F, but they do bind strongly to (BSO *n* = 0.648–1.046) and pull charge from the central I. The effect of the equatorial ligand causes the difference in bond strength between $PhIF_2$ and IF_2^-. IF_2^- has no equatorial ligand and less polar bonds than the 3c–4e bond in $PhIF_2$. When replacing a F with a Ph group (**1.3**), the negative charge becomes localized in the fluorine due to its higher electronegativity; as a result, two different types of bond are formed: one is the 2c–2e C–I bond, and the other is an XB between I and F^- (the lower polarizing power of Ph results in a less positive charge at the iodine).

Figure 2b shows Y$\cdots$I$\cdots$A (where A = F, Cl, Br, and I in this case) in **2.1–2.10**. In the case of $PhIY_2$ (**2.1–2.4**), there is a correlation between bond strength and bond polarity. Charge on the central I atom increases in the series: $PhI_3 < PhIBr_2 < PhICl_2 < PhIF_2$. This matches the trend in 3c–4e bond strength. Charge on the axial ligand also matches this order, but with charge becoming more negative. In **2.5–2.10**, there is a marked difference in I$\cdots$F bond strength (BSO *n* > 0.562) and all other axial bonds (BSO *n* = 0.272–0.423). I$\cdots$Cl, I$\cdots$Br, and I$\cdots$I interactions are similar in bond strength, but vary slightly depending on the atom on the opposite side of the 3c–4e bond. This result is in accord with observed bond polarity and electronegativity trends of halogens.

Figure 3a shows BSO *n* plots for Y$\cdots$IA and Figure 3b YI$\cdots$A in **Groups 3–4**. The same trend emerges again when replacing one halogen with an electron-donating functional group; the bond strength of I$\cdots$A increases when A changes from I to F. Keeping the Y constant and substituting A again reproduce the trend that bonds become stronger when going up the periodic table from I to F for all five functional groups. When comparing the functional groups, bond strength follows this order: $OCO > OC(CH_3)_2 > OH > CN > NH_2$. This order holds regardless of the axial halogen. This pattern nearly matches the order observed in group charges where the more negatively-charged the group, the higher the BSO *n*. The exception is OH and $OC(CH_3)_2$. OH groups are more negatively charged, but do not bind as strongly as $OC(CH_3)_2$ groups. This is because the benzene in **4.5–4.8** binds more strongly on average in **Group 4** (BSO *n* = 0.898–1.046) than Ph in **Group 2** (BSO *n* = 0.691–0.914) and Ph in **Group 3** (BSO *n* = 0.648–0.893). The stronger equatorial bond correlates to a more positive charge on the central I, which allows for stronger 3c–4e bonds. The key difference between **Group 4** and **Groups 2–3** is that all of **Group 4** has functional groups bound directly to benzene and **Groups 2–3** do not. In this case, it is justifiable to state that the $C(CH_3)_2$ group in **4.5–4.8** will be an electron donor to benzene, which accounts for the lower group charge. **2.1** and **3.8** are the only exceptions to this trend.
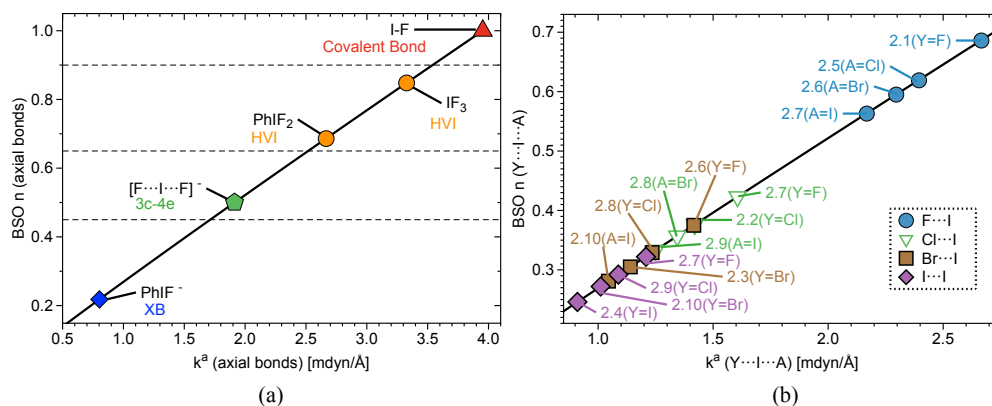
Figure 2. (**a**) Power relationship between bond strength order (BSO) *n* and k^a of **Group 1** bonds (axial bonds only in the case of PhIF$^-$, PhIF$_2$, and IF$_3$) according to eq 2 and (**b**) BSO *n* versus k^a of Y$\cdots$I$\cdots$A bonds for complexes **2.1–2.10**, where Y and A are halogen atoms.

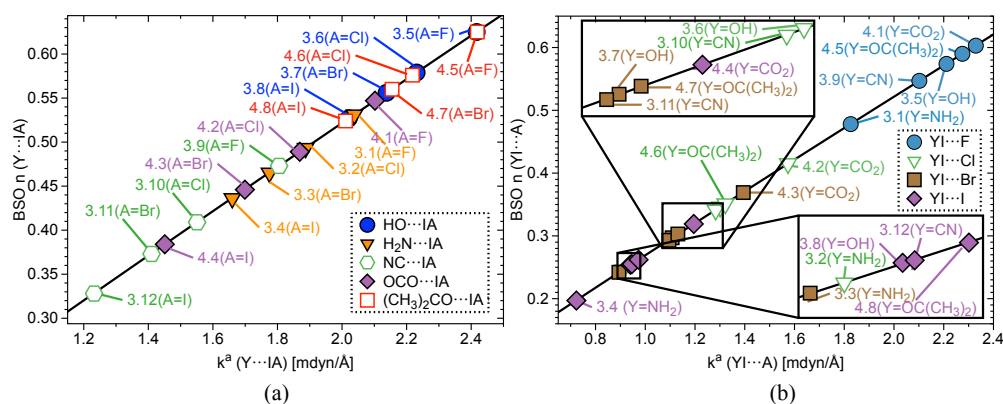**Figure 3.** (**a**) BSO *n* versus for k^a of Y$\cdots$IA (**3.1–4.8**) (**b**) and BSO *n* versus k^a of YI$\cdots$A for complexes **3.1–4.8** according to eq 2, where A = the axial halogen atom and Y = the non-halogen atom bound axial to I.
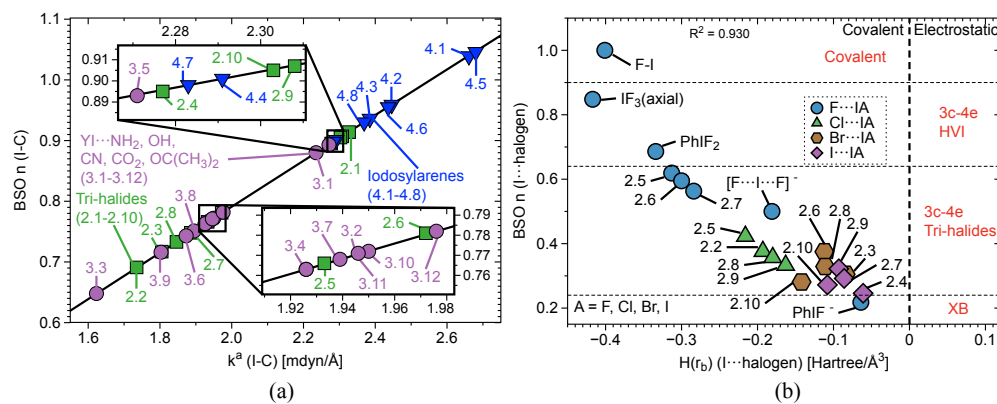

Figure 4. (**a**) BSO *n* versus (k^a) of I–Ph (**2.1–3.12**) and I-benzene (**Group 4**) according to eq 2. BSO *n* for the equatorial I–C bonds has been scaled by a factor of 1.517. (**b**) Comparison of BSO *n* with $H(\mathbf{r}_b)$ of all halogen–iodine interactions in complexes **1.1–2.10**. The vertical dashed line separates the electrostatic region from the covalent region.

Table 1. Bond distance (r), k^a, ω^a, BSO n, $\rho(r_b)$, $H(r_b)$, and %3c–4e for Y–I (**1.1**), Y–I$\cdots$A (**1.3**), and Y$\cdots$I$\cdots$A bonds in **1.2**, **1.4–4.8**, where Y = A in **2.1–2.4**, Y–I = the stronger of the two axial bonds in **1.3** and **2.5–4.8**.

	#	Bond Analyzed (Y–I; I–A)	r (Y–I)	k^a (Y–I)	BSO n (Y–I)	ω^a (Y–I)	$\rho(r_b)$ (Y–I)	$H(r_b)$ (Y–I)	r (I–A)	k^a (I–A)	BSO n (I–A)	ω^a (I–A)	$\rho(r_b)$ (I–A)	$H(r_b)$ (I–A)	%3c–4e
Group1	1.1	F–I	1.921	3.953	1.000	637	0.900	−0.401	-	-	-	-	-	-	-
	1.2	F–I; I–F	2.089	1.913	0.500	443	0.615	−0.181	2.089	1.913	0.500	443	0.615	−0.181	100
	1.3	C–I; I–F	2.173	1.843	0.482	534	0.761	−0.359	2.282	0.803	0.218	287	0.428	−0.064	45
	1.4	F–I; I–F	1.951	3.327	0.848	585	0.875	−0.417	1.951	3.327	0.848	585	0.875	−0.417	100
Group2	2.1	F–I; I F	1.997	2.666	0.686	523	0.783	−0.334	1.997	2.666	0.686	523	0.783	−0.334	100
	2.2	Cl–I; I–Cl	2.481	1.420	0.376	297	0.542	−0.193	2.481	1.420	0.376	297	0.542	−0.193	100
	2.3	Br–I; I–Br	2.651	1.140	0.305	155	0.465	−0.136	2.651	1.140	0.305	155	0.465	−0.136	100
	2.4	I–I; I–I	2.892	0.910	0.246	199	0.380	−0.092	2.892	0.904	0.244	156	0.380	−0.092	100
	2.5	F–I; I–Cl	2.014	2.395	0.619	496	0.759	−0.313	2.454	1.606	0.423	315	0.567	−0.216	68
	2.6	F–I; I–Br	2.025	2.296	0.595	486	0.745	−0.300	2.606	1.416	0.375	222	0.503	−0.164	63
	2.7	F–I; I–I)	2.039	2.168	0.563	472	0.725	−0.284	2.821	1.208	0.322	180	0.431	−0.123	57
	2.8	Cl–I; I–Br	2.498	1.344	0.357	288	0.525	−0.180	2.632	1.235	0.329	208	0.481	−0.147	92
	2.9	Cl–I; I–I	2.522	1.250	0.333	278	0.503	−0.163	2.847	1.088	0.292	171	0.412	−0.111	88
	2.10	Br–I; I–I	2.677	1.045	0.281	191	0.443	−0.121	2.865	1.011	0.272	164	0.399	−0.103	97
Group 3	3.1	N–I; I–F	2.080	2.038	0.531	524	0.854	−0.481	2.084	1.826	0.478	433	0.654	−0.228	90
	3.2	N–I; I–Cl	2.087	1.887	0.493	504	0.851	−0.472	2.611	0.911	0.246	238	0.419	−0.110	50
	3.3	N–I; I–Br	2.100	1.775	0.465	489	0.835	−0.456	2.767	0.894	0.242	177	0.371	−0.084	52
	3.4	N–I; I–I	2.113	1.660	0.436	473	0.817	−0.437	2.998	0.723	0.197	139	0.315	−0.061	45
	3.5	O–I; I–F	2.031	2.417	0.625	537	0.836	−0.435	2.036	2.275	0.590	483	0.722	−0.283	94
	3.6	O–I; I–Cl	2.042	2.231	0.579	516	0.822	−0.419	2.520	1.301	0.346	284	0.500	−0.165	60
	3.7	O–I; I–Br	2.051	2.138	0.556	505	0.761	−0.365	2.676	1.108	0.297	197	0.425	−0.112	53
	3.8	O–I; I–I	2.064	2.021	0.527	491	0.790	−0.388	2.895	0.940	0.254	159	0.378	−0.093	48
	3.9	F–I; I–C	2.038	2.211	0.574	476	0.722	−0.282	2.154	1.805	0.473	529	0.763	−0.388	82
	3.10	C–I; I–Cl	2.174	1.551	0.409	490	0.705	−0.334	2.519	1.283	0.341	282	0.474	−0.147	83
	3.11	C–I; I–Br	2.189	1.410	0.373	467	0.681	−0.311	2.672	1.095	0.293	195	0.421	−0.111	79
	3.12	C–I; I–I	2.213	1.232	0.328	437	0.644	−0.279	2.887	0.946	0.255	159	0.365	−0.086	78
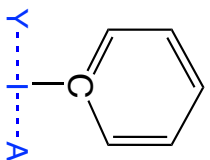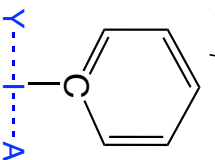
Table 1. *Cont.*

#	Bond Analyzed (Y–I; I–A)	r (Y–I)	k^a (Y–I)	BSO n (Y–I)	ω^a (Y–I)	$\rho(r_b)$ (Y–I)	$H(r_b)$ (Y–I)	r (I–A)	k^a (I–A)	BSO n (I–A)	ω^a (I–A)	$\rho(r_b)$ (I–A)	$H(r_b)$ (I–A)	%3c–4e
Group 4														
4.1	F–I; I–O	1.993	2.622	0.675	519	0.757	−0.313	2.079	2.102	0.547	501	0.719	−0.325	81
4.2	O–I; I–Cl	2.102	1.869	0.489	473	0.682	−0.291	2.448	1.574	0.415	312	0.536	−0.190	85
4.3	O–I; I–Br	2.117	1.699	0.446	451	0.657	−0.269	2.598	1.394	0.369	221	0.473	−0.142	83
4.4	O–I; I–I	2.141	1.451	0.384	416	0.623	−0.238	2.809	1.195	0.319	179	0.408	−0.108	83
4.5	O–I; I–F	2.032	2.419	0.625	538	0.800	−0.403	2.024	2.329	0.603	489	0.710	−0.274	96
4.6	O–I; I–Cl	2.041	2.218	0.576	515	0.781	−0.384	2.503	1.322	0.351	286	0.482	−0.153	61
4.7	O–I; I–Br	2.050	2.155	0.560	507	0.763	−0.367	2.658	1.131	0.303	199	0.424	−0.113	54
4.8	O–I; I–I	2.063	2.011	0.524	490	0.739	−0.343	2.875	0.973	0.262	161	0.364	−0.085	50

[a] Calculated at the ωB97X-D/aug-cc-pVTZ level of theory. r are given in Å, $\rho(r_b)$ in e/Å³, $H(r_b)$ in Hartree/Å³, k^a in mdyn/Å, BSO n, %3c–4e calculated in terms of BSO n, and ω^a in cm⁻¹. In **Group 4**, R = CO (**4.1**–**4.4**). For **4.5**–**4.8**, R = C(CH₃)₂.
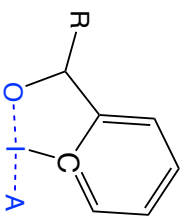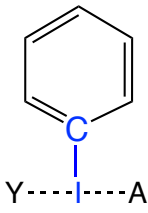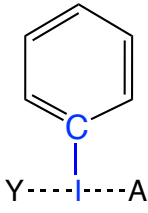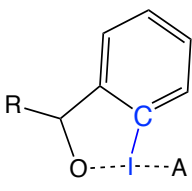
Table 2. r, $\rho(\mathbf{r}_b)$, $H(\mathbf{r}_b)$, and local vibrational data for I-equatorial ligand (I–F, I–C) interactions of complexes **1.4–4.8**, where BSO *n* is scaled by a factor of 1.517.

	#	Bond Analyzed	r	$\rho(\mathbf{r}_b)$	$H(\mathbf{r}_b)$	k^a	BSO *n* (*Scaled*)	ω^a
Group 1	**1.4**	I–F	1.876	1.037	−0.569	4.087	1.565	648
Group 2	**2.1**	I–C	2.123	0.895	−0.476	2.327	0.914	600
	2.2	I–C	2.116	0.895	−0.476	1.735	0.691	518
	2.3	I–C	2.107	0.905	−0.488	2.277	0.717	594
	2.4	I–C	2.107	0.901	−0.484	1.805	0.895	529
	2.5	I–C	2.129	0.880	−0.461	1.933	0.766	547
	2.6	I–C	2.125	0.884	−0.466	1.972	0.781	553
	2.7	I–C	2.120	0.891	−0.473	1.886	0.748	540
	2.8	I–C	2.112	0.900	−0.482	1.846	0.733	535
	2.9	I–C	2.103	0.912	−0.495	2.308	0.907	598
	2.10	I–C	2.105	0.907	−0.490	2.303	0.905	597
Group 3	**3.1**	I–C	2.139	0.869	−0.452	2.235	0.880	588
	3.2	I–C	2.157	0.836	−0.418	1.950	0.772	549
	3.3	I–C	2.142	0.858	−0.44 0	1.623	0.648	501
	3.4	I–C	2.132	0.872	−0.455	1.926	0.763	546
	3.5	I–C	2.128	0.888	−0.471	2.271	0.893	593
	3.6	I–C	2.133	0.874	−0.457	1.895	0.751	542
	3.7	I–C	2.130	0.834	−0.424	1.939	0.768	548
	3.8	I–C	2.125	0.885	−0.468	1.873	0.743	538
	3.9	I–C	2.138	0.865	−0.445	1.803	0.716	528
	3.10	I–C	2.130	0.822	−0.402	1.926	0.763	546
	3.11	I–C	2.127	0.829	−0.409	1.946	0.771	549
	3.12	I–C	2.123	0.841	−0.421	1.976	0.782	553
Group 4	**4.1**	I–C	2.090	0.907	−0.490	2.661	1.039	642
	4.2	I–C	2.110	0.863	−0.445	2.446	0.959	615
	4.3	I–C	2.115	0.852	−0.434	2.385	0.936	608
	4.4	I–C	2.123	0.838	−0.421	2.291	0.901	596
	4.5	I–C	2.094	0.901	−0.485	2.680	1.046	644
	4.6	I–C	2.113	0.860	−0.444	2.436	0.955	614
	4.7	I–C	2.118	0.851	−0.434	2.369	0.930	606
	4.8	I–C	2.124	0.838	−0.422	2.283	0.898	594

[a] Calculated at the ωB97X-D/aug-cc-pVTZ level of theory. r are given in Å, $\rho(\mathbf{r}_b)$ in e/Å^3, $H(\mathbf{r}_b)$ in Hartree/Å^3, k^a in mdyn/Å, BSO *n*, and ω^a in cm^{-1}. In **Group 4**, R = CO (**4.1–4.4**). For **4.5–4.8**, R = C(CH$_3$)$_2$.

2.3. Covalent/Electrostatic Contributions

Figures 4b and 5 contain three plots correlating BSO *n* with $H(\mathbf{r}_b)$ of I$\cdots$axial halogens in **Group 2** (Figure 4b), Y$\cdots$IA in **Groups 3–4** (Figure 5a), and YI$\cdots$A in **Groups 3–4** (Figure 5b). The vertical dashed line through the origin separates the covalent region from the electrostatic region according to the Cremer–Kraka criterion. $H(\mathbf{r}_b) < 0$ for every I–A, I–Y, and I–C equatorial (Ph, F, or benzene) interaction, putting them in the covalent bonding region or very close to the electrostatic region in some cases. There is significant covalent contribution for the axial bonding interactions in **2.1–4.8**, indicating that charge accumulation in the bonding region produces a net stabilizing effect. For the plot in Figure 4b, there is a good linear correlation between BSO *n* and $H(\mathbf{r}_b)$, as indicated by a value of $R^2 = 0.930$. These data correlate higher bond strength to an increase in covalent character of the interaction. The weaker the bond, the closer to the electrostatic region. The plot is sectioned off into regions to show agreement with Figure 2a. The XB interaction in PhIF$^-$ is at the bottom of the plot, closest to the electrostatic region. The 3c–4e region is next, where IF$_2^-$ is found, along with all of the weakly-bound λ^3-iodanes containing axial Cl, Br, and I atoms. It is necessary to note that we expect the 3c–4e bond in IF$_2^-$ to be the strongest of all trihalides and to be at the very top of the spectrum. Therefore, if considering other trihalide systems, one would expect to see better separation between 3c–4e bonds in HVI and 3c–4e bonds in trihalides, as is observed for the more closely-related IF$_2^-$,

PhIF$_2$, and IF$_3$. All of the λ^3-iodanes containing F are at the very top of this region bordering the next region or in the next region, which is 3c–4e HVI. IF$_3$ and PhIF$_2$ give prime examples of the 3c–4e HVIB. At the very top right corner is the covalent F–I complex. As we follow the linear data from the weak electrostatic region to the strong covalent region, we once again reproduce the smooth continuum: partially-covalent XB < 3c–4e bond in trihalides < 3c–4e bond in HVI < covalent bond. Now, the trend holds in terms of covalent/electrostatic character and $H(\mathbf{r}_b)$. Note that in Figures 4 and 5, $\rho(\mathbf{r}_b)$ could be plotted against BSO n in place of $H(\mathbf{r}_b)$, and the same correlation would occur, but with a positive slope instead of a negative one.

The same general trend is observed in Figure 5 for **Groups 3–4**. As BSO n increases, $H(\mathbf{r}_b)$ becomes more negative (deeper into the covalent region). In Figure 5a, points for Y$\cdots$I are scattered, and the correlation weakens when taking the data as a whole. However, if considering each functional group individually, a strong linear correlation once again occurs. The periodic trend emerges that as A, the halogen homolog becomes smaller, the bond strengthens and becomes more covalent in nature. This is not a direct result of the axial ligand, rather it is the result of the polarizing effect the axial halogen has on the central I atom. The Y$\cdots$IA interactions ($H(\mathbf{r}_b) < -0.237$ Hartree/Å^3) sit significantly farther into the covalent region compared to the YI$\cdots$A interactions ($H(\mathbf{r}_b) < -0.055$ Hartree/Å^3). Figure 5b again shows a reasonable linear correlation with $R^2 = 0.917$. The trend amongst functional groups previously noted in **3.1–3.2** is once again evident here: OCO > OC(CH$_3$)$_2$ > OH > CN > NH$_2$ in terms of pulling charge from the central I, which results in strengthening and to some degree increasing $H(\mathbf{r}_b)$ of the I$\cdots$A bond. Another important point here is that one must not assume certain functional groups will behave the same way in all situations as they behave when bound to benzene. A prime example is CN: a strong electron withdrawing group (when bound to benzene) is the second weakest withdrawing group in this study.
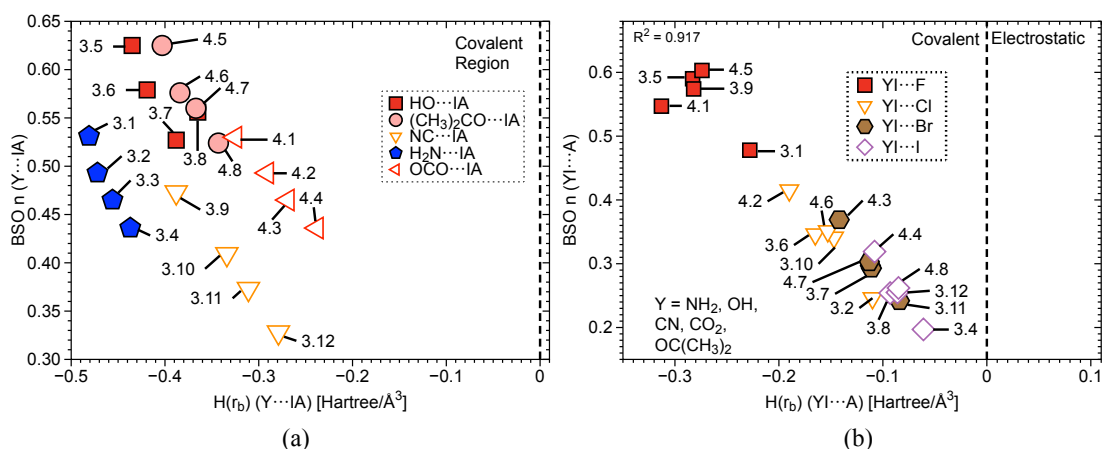

Figure 5. (**a**) Comparison of BSO n with $H(\mathbf{r}_b)$ of iodine-non halogen axial atom (Y$\cdots$IA) interactions in complexes **3.1–4.8** and (**b**) a comparison of BSO n with $H(\mathbf{r}_b)$ of axial halogen-iodine (YI$\cdots$A) interactions in complexes **3.1–4.8**. The vertical dashed line separates the electrostatic region from the covalent region.

2.4. 3c–4e Bonding

%3c–4e bonding character is shown Table 1. Vibrational spectroscopy was utilized to define a new and simple 3c–4e parameter, which was derived from Local Mode Analysis (L-modes). It utilizes BSO n values to define %3c–4e bonding as:

$$\%(3c\text{-}4e) = \frac{BSOn(AI)}{BSOn(YI)} \times 100 \tag{1}$$

where BSO n (Y$\cdots$I) > BSO n (A$\cdots$I). A$\cdots$I is the weaker, less covalent bond, and Y$\cdots$I is the stronger, more covalent bond. In **2.1–2.4**, A = Y; therefore, 3c–4e is 100%. In **2.5–2.7**, %3c–4e decreases from 68% in **2.5** to 57% in **2.7** as ΔBSO n becomes larger. **2.8–2.10** contain weakly-bound halogens, which promote high 3c–4e bonding character (88–97%). In **3.1–3.12**, there is a large range of 3c–4e contributions to the Y$\cdots$I$\cdots$A interactions (45–94%). The highest percentage is in **3.5**, where the 3c–4e interaction is HO$\cdots$I$\cdots$F. Both substituents have lp electrons and are highly electronegative. The bonds formed are strong and polar, as the central I is the most polarized of all **Group 3** molecules with an NBO charge of +1.401 e. OH and F have similar BSO n and NBO charges: n = 0.625, −0.565 e and n = 0.590, −0.703 e, respectively. The **3.1** has high 3c–4e character for the same reason as **3.5**, but with NH$_2$ involved instead of OH. N is slightly less electronegative than O, and NH$_2$ has a more positive charge than OH, and thus forms a slightly weaker, less polar bond. **3.3–3.4** and **3.7–3.8** have the lowest 3c–4e character in **Group 3**. These species contain mostly I–Br or I–I bonds, which bind weakly, while on the other side of the Y$\cdots$I$\cdots$A, we have polar functional groups OH and NH$_2$. There is a strong polar interaction on one side of I and a weak non-polar interaction on the other side, which decreases the 3c–4e character. **4.1–4.4** have high 3c–4e character (81–85%). The I–O oxygen is part of an ester group which carries a large negative charge and contributes resonance stabilization. In **4.5–4.8**, I is bound to the O on a T-butoxy group, which is slightly less electron rich and does not have the benefit of resonance. The T-butoxy-O binds strongly to I compared to Cl, Br, and I.

3. Computational Methods

DFT was utilized to optimize molecular geometries and to calculate for each stationary point molecular vibrational frequencies including the L-modes of Konkoli and Cremer [60–62] and the determination of local mode force constants (k^a), NBO charges, electron densities $\rho(\mathbf{r}_b)$, and energy densities $H(\mathbf{r}_b)$; where $\mathbf{r}_b$ is a bond critical point. Each stationary point was confirmed as a minimum by absence of imaginary normal mode frequencies. Available experimental geometries for the ICl$_3$ dimer, IF$_3$, IF$_5$, dichloroiodobenzene (PhICl$_2$), and diacetoxyiodobenzene (PhI(OAc)$_2$) [18,63–66] were used to gauge the accuracy of the DFT calculations. Experimental and calculated geometries using different model chemistries for this set of compounds are compared in Tables A1 and A2 (See Appendix A). We initially employed Grimme's Rung 5 double hybrid density functional B2PLYP [67] and Dunning's cc-pVDZ basis set [68–71] with a tight convergence criterion and an ultra-fine integration grid. The B2PLYP functional combines the generalized gradient approximation exchange functional of Becke [72,73] and the Lee–Yang–Parr correlation functional [74] with exact Hartree–Fock exchange and Møller–Plesset perturbation theory [75–78] of second order (MP2) [79–81]. This functional has shown close agreement between calculated and experimental geometries and vibrational frequencies for heavy atoms [82,83]. However, for our set of molecules, the cc-pVDZ basis set did not produce the desired accuracy (Tables A1 and A2), and the B2PLYP/aug-cc-pVTZ level of theory became computationally expensive. The combination of MP2 and a relatively small double-zeta basis set is known to provide a fortuitous cancellation of error [84,85]. MP2 overestimates correlation energy, but this is compensated by the cc-pVDZ basis set [86]. Therefore, we tested MP2/cc-pVDZ for reducing the computer time. However, results calculated at this level of theory gave less accurate results than ωB97X-D/aug-cc-pVTZ [87,88], while calculations at the B2PLYP/Def2TZP level of theory led to inaccurate results in several cases. For Br and I, scalar relativistic effects were assessed by using effective core potentials (ECPs) in combination with the Dunning basis sets [89,90].

Although geometries are first order properties and therefore less sensitive to the level of theory, B2PLYP/aug-cc-pVTZ and ωB97X-D/aug-cc-pVTZ calculations turned out to be in closest agreement with experimental data, while for a small subset of compounds, close agreement between ωB97X-D/aug-cc-pVTZ and CCSD(T)/aug-cc-pVTZ was obtained (Table A3). To further rationalize these results, gauge-independant atomic orbital (GIAO) magnetic shielding tensors [91–95] were calculated and isotropic shielding constants were converted into chemical shifts utilizing the linear regression method of Tantillo et al. for PhICl$_2$, PhI(OAc)$_2$, and 1-Hydroxy-1,2-benziodoxol-3(1H)-one [96–101]. This

method requires the calculation of isotropic magnetic shielding tensors for a test set of molecules at a given level of theory (in our case, ωB97X-D/aug-cc-pVTZ and B3LYP/aug-cc-pVTZ), plotting the raw calculated isotropic value against experimental NMR chemical shifts, and using the following relationship to develop an equation for calculating chemical shifts (Figure A1):

$$\delta = \frac{(y - intercept) - \sigma}{-slope} \tag{2}$$

where δ is the derived chemical shift and σ is the calculated isotropic magnetic shielding tensor. The margin of error for proton-NMR chemical shifts turned out to be 0.24–6.91% for the B3LYP functional and 0.19–5.81% for the ωB97X-D functional (Table A4) [18,63,102]. Although both ωB97X-D and B3LYP gave satisfactory and similar calculated chemical shifts, ωB97X-D gave more accurate geometries and frequencies.

Based on these findings, the ωB97X-D/aug-cc-pVTZ level of theory was chosen for this study due to its displayed ability to predict accurate first and second order experimental properties in HVI molecules in addition to the previous findings of Oliveira et al. that this level of theory is suitable for the detailed analysis of XB [41].

Vibrational spectroscopy was applied to quantify the intrinsic strength of HVIBs. Chemists have utilized vibrational spectroscopy to obtain information about the electronic structure of molecules and their framework of bonds. However, normal vibrational modes cannot be used as a direct bond strength measure because they are delocalized due to electronic and mass coupling, a fact that often has been overlooked [103,104]. The electronic coupling is eliminated by solving the Wilson equation of spectroscopy [105] and transforming to normal coordinates. Konkoli and Cremer showed that the remaining mass (kinematic) coupling can be eliminated by solving a mass-decoupled equivalent of the Wilson equation, leading to local vibrational modes, which are associated with internal coordinates q_n such as bond lengths, bond angles, and dihedral angles [60,106]. Zou and Cremer verified that there is a one-to-one relationship between local and normal vibrational modes through an adiabatic connection scheme (ACS) [107–109], allowing a normal mode decomposition into local mode contributions [44,110,111] and, as such, the detailed analysis of a vibrational spectrum. This is of particular value, given the fact that L-modes can be applied to both calculated and measured spectra [61,112].

Another important feature of L-modes is the direct relationship between the local stretching force constant (k^a) of a chemical bond and its intrinsic strength [113]. This has enhanced our knowledge about chemical bonding and the often overlooked, but highly important weak intermolecular interactions, providing a wealth of new insight into: (i) covalent bonding [113], stretching from peculiar cases of reversed bond length-bond strength relationships [114,115], to a new design recipe for fluorinating agents [116]; (ii) weak chemical interactions including hydrogen bonding [117,118], XB [35,41,42], pnicogen bonding [43], chalcogen bonding [50], weak interactions in gold clusters [119], as well as non-classical hydrogen bonds in boron–hydrogen $\cdots \pi$ interactions [120,121]. In addition, new electronic parameters and rules were derived [122–124].

When comparing a larger set of k^a, the use of a relative bond strength order (BSO n) is convenient [103,104]. The BSO n of a bond is obtained by utilizing the extended Badger rule [103,104,125] according to which BSO n is related to k^a by a power relationship, which is fully determined by two reference values and the requirement that for a zero-force constant, the BSO n value becomes zero:

$$\text{BSO } n = a(k^a)^b \tag{3}$$

The constants a and b are calculated from k^a values of two reference compounds with known BSO n values n_1 and n_2 via:

$$a = n_2/(k_2^a)^b \tag{4}$$

and,

$$b = ln(n_2/n_1)/ln(k_2^a/k_1^a) \tag{5}$$

In this work, we chose as reference compounds FI and IF_2^- representing BSO n values of one and 0.5, respectively, guided by the corresponding Mayer bond orders [126] of 0.940 and 0.543 evaluated at the ωB97X-D/cc-pVTZ level of theory. More than 50% of iodine bonds in this work include an atom from the second period. This renders the FI/IF_2^- reference system ideal (a second period atom bound to iodine), in addition to providing a spectrum with a full 3c–4e bond from a trihalide (IF_2^-) on the one end and a full covalent bond (FI) on the other end.

Using the k_1^a of 1.913 mdyn/Å for IF_2^- and 3.953 mdyn/Å for FI (ωB97X-D/cc-pVTZ level of theory), the constants a and b in the power relationship Equation (3) were determined to be $a = 0.269$ and $b = 0.955$, leading to:

$$\text{BSO } n = 0.269(k^a)^{0.955} \tag{6}$$

Because the chosen reference system was designed for 3c–4e interactions particular to this study, a scaling procedure was used to obtain appropriate BSO n values for covalent I–C interactions between the equatorial ligands and the central iodine. The equatorial bonds are fully-formed single bonds, but the C–I bond is much less polar and weaker than the I–F bond used as a reference. We calculated $k^a = 2.557$ mdyn/Å for the I–C bond in iodobenzene. From Equation (6), we calculated BSO $n = 0.659$. The scaling factor was obtained by setting $n = 1$ for this I–C bond. The scaling factor is $1/0.659 = 1.517$, which was applied to BSO n of all equatorial I–C bonds. Multiplying the scaling factor through Equation (6) provided a new BSO n equation for assessing the strength of the equatorial I–C bonds in this study:

$$\text{BSO } n(scaled) = 0.408(k^a)^{0.955} \tag{7}$$

The Cremer–Kraka criterion was applied to assess the covalent nature of HVIB [42,55,56,77,127]. According to this criterion, a covalent bond between two atoms A and B is defined by (1) the existence of a zero-flux surface and bond critical point ($\mathbf{r}_b$) between atoms A and B (*necessary condition*) and (2) a negative and thereby stabilizing local energy density $H(\mathbf{r}_b)$ (*sufficient condition*). $H(\mathbf{r}_b)$ will be close to zero or positive if the interaction between A and B is non-covalent, that is electrostatic or of the dispersion type. $H(\mathbf{r})$ is defined as:

$$H(\mathbf{r}) = G(\mathbf{r}) + V(\mathbf{r}) \tag{8}$$

where $G(\mathbf{r})$ is the kinetic energy density (always positive, destabilizing) and $V(\mathbf{r})$ is the potential energy density (always negative, stabilizing). In addition to the established Cremer–Kraka criterion, a molecular fragmentation scheme for estimating electron density shifts has recently emerged as a potential tool for the qualitative investigation of non-covalent interactions at low computational cost [128].

L-modes was carried out with the program COLOGNE2018 [129], and Mayer bond orders were determined with the program ORCA [130]. NBO populations were computed using NBO 6 [131–134]. The electron density analysis, in particular the calculation of electron density at the bond critical point ($\rho(\mathbf{r}_b)$) and $H(\mathbf{r}_b)$, was performed with the program AIMAll [135,136]. All DFT calculations were carried out with GAUSSIAN16 [137].

4. Conclusions

In this work, we quantified the intrinsic bond strength and bonding nature of a series of HVI compounds through vibrational spectroscopy. Use of DFT in this work was rationalized by testing several levels of theory against first and second order experimental properties of a small set of known HVI reagents. The computed set of 34 HVI molecules was then compared to XB, 3c–4e bonding, and covalent bonding in terms of BSO n, k^a, $\rho(\mathbf{r}_b)$, $H(\mathbf{r}_b)$, and NBO charges. Recently, Politzer and coworkers [138] showed that by substituting a ligand in trihalides with a negative point charge, the positive electrostatic potential at the polarized σ-hole collinear to the point charge correlates

qualitatively well with the interaction energy; substantiating the key role played by electrostatics, which is also reflected in the atomic charge distribution (see Figure 1) and can be rationalized in terms of the 3c–4e model. The more negative charge at the ligands Y and A compared to the central iodine is due to the presence of a node at the center of the occupied non-bonding orbital [139]. This charge separation is responsible for the lower covalent character of 3c–4e bonds compared to a classical 2c–2e bond. Politzer and coworkers proposed the existence of a continuum between non-covalent and covalent bonds, the latter being a result of an increased degree of polarization [138]. Our results do also suggest the existence of such a continuum, but whether covalency can be seen as a degree of polarization is still disputable, especially in view of Ruedenberg's description of covalent bonding, where energy lowering is a result of the complex interplay of kinetic and potential energy contributions [140,141]. The 3c–4e bonds in HVI share properties with XB, but are more closely related to the 3c–4e bonds in trihalides or covalent bonding in extreme cases. The equatorial 2c–2e HVI bond is stronger than comparable 3c–4e bonds (bonds involving the same ligands like in IF_3) and is more closely related to a covalent bond. Our results support the following transition: XB < 3c–4e bond in trihalides < 3c–4e bond in HVI < 2c–2e bond in $PhIF_2$ < covalent bond. When comparing the difference (equatorial ligands) between trihalides and λ^3-iodanes, we found that the 3c–4e HVIB is strengthened by the equatorial ligand by comparing IF_2^-, $PhIF_2$, and IF_3. The equatorial ligand contributes significantly in pulling electron density from the central I, allowing for more polar interactions. Thus, highly electronegative ligands at the equatorial position will form strong interactions, as will axial ligands in such a case. We also found that axial ligands in HVIs have a minimal direct effect on one another in terms of NBO charge analysis, but do play a role in altering charge on the central I. Substituent effects in HVI can alter bond strength in both axial ligands and the equatorial ligand, particularly when F atoms are involved as ligands. The five functional groups studied here play a bond-strengthening and -polarizing role in the following order: OCO > $OC(CH_3)_2$ > OH > CN > NH_2, with OH and $OC(CH_3)_2$ being partially interchangeable. In terms of $H(\mathbf{r}_b)$, we found a strong linear correlation with BSO n. $H(\mathbf{r}_b)$ becoming more negative correlates to an increase in bond strength. Furthermore, large $V(\mathbf{r})$ stabilization in the bonding region correlates to the increased covalent character of a bond. Finally, we found the 3c–4e bond concept to be a valuable descriptor in terms of the linear portion of λ^3-iodanes.

　　　Future goals are to utilize L-modes and the analysis of the electrostatic potential to explain why the T-shaped molecular geometry in λ^3-iodanes contains improper dihedrals and non-ideal bond angles. We also plan to investigate 3c–4e bonding and intramolecular HB in a series of HVI reagents utilizing L-modes and to explore the chemical reactivity of HVI compounds utilizing the unified reaction valley approach developed in our group [103,142–144]. In addition, we will perform a conformational and geometrical study of a series of novel HVI monomeric materials with a strong potential of forming useful polymers [145,146].

Conflicts of Interest: The authors declare no conflict of interest.

Appendix A

　　　Table A1 shows bond lengths, bond angles, and % error compared to experimentally measured data for IF_3, IF_5, and $(ICl_3)_2$. For each molecule, geometry optimizations and vibrational frequencies were calculated at the B2PLYP/cc-pVDZ, B2PLYP/aug-cc-pVTZ, B2PLYP/Def2TZP, B3LYP/aug-cc-pVTZ, ωB97X-D/aug-cc-pVTZ, and M2P/cc-pVDZ levels of theory.

B2PLYP/aug-cc-pVTZ and ωB97X-D/aug-cc-pVTZ levels of theory give superior results for the given geometry parameters. Table A2 shows bond lengths, bond angles, and % error compared to experimentally measured data for PhICl$_2$ and PhI(OAc)$_2$ computed at all of thee aforementioned levels of theory. These two molecules are similar, or the same in the case of PhICl$_2$ as the majority of the molecules in this work. The ωB97X-D/aug-cc-pVTZ gave remarkable accuracy in calculating geometry parameters for these two molecules.

Table A1. Calculated and experimental bond lengths and bond angles for the (ICl$_3$)$_2$ dimer, IF$_5$, and IF$_3$, showing B2PLYP and ωB97X-D/aug-cc-pVTZ levels of theory giving closest agreement with the experiment [64–66].

Method Basis Set	r_1 (I–Cl, F) [Å]	% Error	r_2 (I–Cl, F) [Å]	% Error	$\theta_{(F–I–F)}$ Degrees	% Error
(ICl$_3$)$_2$ B2PLYP						
cc-pVDZ	2.432	1.97	2.770	1.83	N/A	N/A
aug-cc-pVTZ	2.397	0.50	2.733	0.48	N/A	N/A
Def2TZP	2.448	2.64	2.773	1.95	N/A	N/A
B3LYP						
aug-cc-pVTZ	2.412	1.13	2.758	1.40	N/A	N/A
ωB97X-D						
aug-cc-pVTZ	2.364	0.88	2.744	0.88	N/A	N/A
MP2						
cc-pVDZ	2.420	1.47	2.746	0.96	N/A	N/A
Experiment	2.385	N/A	2.720	N/A	N/A	N/A
IF$_5$						
B2PLYP						
cc-pVDZ	1.900	3.04	1.941	3.85	N/A	N/A
aug-cc-pVTZ	1.847	0.16	1.908	2.09	N/A	N/A
Def2TZP	1.859	0.81	1.919	2.68	N/A	N/A
B3LYP						
aug-cc-pVTZ	1.857	0.70	1.918	2.62	N/A	N/A
ωB97X-D						
aug-cc-pVTZ	1.840	0.22	1.901	1.71	N/A	N/A
MP2						
cc-pVDZ	1.895	2.77	1.933	3.42	N/A	N/A
Experiment	1.844	N/A	1.869	N/A	N/A	N/A
IF$_3$						
B2PLYP						
cc-pVDZ	1.931	3.15	1.984	0.05	169.2	5.55
aug-cc-pVTZ	1.885	0.69	1.960	1.16	167.7	4.61
Def2TZP	1.900	1.50	1.975	0.40	168.6	5.18
B3LYP						
aug-cc-pVTZ	1.900	1.50	1.975	0.40	168.6	5.18
ωB97X-D						
aug-cc-pVTZ	1.876	0.21	1.951	1.61	167.5	4.49
MP2						
cc-pVDZ	1.925	2.83	1.977	0.30	168.2	4.93
Experiment	1.872	N/A	1.983	N/A	160.3	N/A

Table A2. Calculated and experimental bond lengths and bond angles for $PhICl_2$ and $PhI(OAc)_2$ showing B2PLYP/aug-cc-pVTZ and ωB97X-D/aug-cc-pVTZ levels of theory giving closest agreement with the experiment [18,63].

| Method Basis Set	r_1 (I–Cl, O) [Å]	% Error	r_2 (I–C) [Å]	% Error	$\theta_{(Cl,O)-I-(O,C)}$ Degrees	% Error
$PhICl_2$						
B2PLYP						
cc-pVDZ	2.536	2.26	N/A	N/A	90.5	1.46
aug-cc-pVTZ	2.505	1.01	N/A	N/A	89.6	0.45
Def2TZP	2.558	3.15	N/A	N/A	89.8	0.67
B3LYP						
aug-cc-pVTZ	2.524	1.77	N/A	N/A	90.3	1.23
ωB97X-D						
aug-cc-pVTZ	2.481	0.04	N/A	N/A	89.2	0.00
MP2						
cc-pVDZ	2.517	1.49	N/A	N/A	88.9	0.34
Experiment	2.480	N/A	N/A	N/A	89.2	N/A
$PhI(OAc)_2$						
B2PLYP						
cc-pVDZ	2.212	2.60	2.150	2.87	164.5	0.30
aug-cc-pVTZ	2.178	1.02	2.081	0.43	162.8	0.73
Def2TZP	2.179	1.07	2.111	1.00	163.1	0.55
B3LYP						
aug-cc-pVTZ	2.194	1.76	2.124	1.63	163.7	0.18
ωB97X-D						
aug-cc-pVTZ	2.149	0.32	2.104	0.67	162.9	0.66
MP2						
cc-pVDZ	2.187	1.44	2.122	1.53	162.7	0.79
Experiment	2.156	N/A	2.090	N/A	164.0	N/A

Table A3 compares computed bond lengths and k^a for FI, IF_2^-, IF_3, and IF_5 at the ωB97X-D/CCSD(T)/aug-cc-pVTZ level of theory. Once again, ωB97X-D/aug-cc-pVTZ performs remarkably well compared to the gold standard CCSD(T). Table A4 shows calculated and experimental NMR shifts for $PhICl_2$, $PhI(OAc)_2$, and 1-hydroxy-1,2-benziodoxol-3(1H)-one using the B3LYP and ω97X-D functionals with the aug-cc-pVTZ basis set. Figure A1 shows a strong linear correlation between calculated isotropic magnetic stretching tensors and experimentally measured chemical shifts. The calculations done at the ωB97X-D/aug-cc-pVTZ level of theory are slightly more in agreement with experimental measurements than the B3LYP/aug-cc-pVTZ.

Table A3. Calculated r and k^a of all FI bonds in FI, IF_2^-, IF3, and IF5 computed at the ωB97X-D/CCSD(T)/aug-cc-pVTZ level of theory.

Molecule Level of Theory	r (FI) Equatorial (Å)	k^a (FI) Equatorial (mdyn/Å)	r (FI) Axial (Å)	k^a (FI) Axial (mdyn/Å)
FI				
ωB97X-D/aug-cc-pVTZ	1.921	3.953	-	-
CCSD(T)/aug-cc-pVTZ	1.931	3.705	-	-
$[F\cdots I\cdots F]^-$				
ωB97X-D/aug-cc-pVTZ	2.089	1.913	-	-
CCSD(T)/aug-cc-pVTZ	2.085	1.746	-	-
IF_3				
ωB97X-D/aug-cc-pVTZ	1.876	4.087	1.951	3.327
CCSD(T)/aug-cc-pVTZ	1.878	4.278	1.950	3.325
IF_5				
ωB97X-D/aug-cc-pVTZ	1.840	4.529	1.901	3.634
CCSD(T)/aug-cc-pVTZ	1.840	4.706	1.895	3.834

Table A4. Calculated and experimental NMR chemical shifts for PhICl$_2$, PhI(OAc)$_2$, and 1-hydroxy-1,2-benzodoxol-3(1H)-one computed using the aug-cc-pVTZ basis set [18,63,102].

ωB97X-D				B3LYP		
Magnetic Isotropic Shielding Tensor	δ-Calculated (ppm)	δ-Experimental (ppm)	% Error	Magnetic Isotropic Shielding Tensor	δ-Calculated (ppm)	% Error
PhICl$_2$						
23.64	7.58	7.16	5.51	23.77	7.51	4.65
23.57	7.65	7.40	3.24	23.71	7.57	2.19
23.41	7.79	7.68	1.42	23.57	7.70	0.24
PhIOAc$_2$						
23.42	7.79	8.24	5.81	23.56	7.71	6.91
23.50	7.70	7.68	0.37	23.67	7.61	0.91
23.59	7.62	7.58	0.59	23.74	7.54	0.44
29.68	2.01	1.92	4.72	29.64	2.00	4.02
1-Hydroxy-1,2 -benziodoxol-3(1H)-one						
23.45	7.76	7.71	0.58	23.61	7.66	0.65
22.91	8.26	8.02	2.85	23.04	8.20	2.19
23.20	7.99	7.97	0.19	23.36	7.90	0.90
23.30	7.89	7.85	0.50	23.44	7.82	0.35

(a)　　　　　　　　　　　　　　　(b)
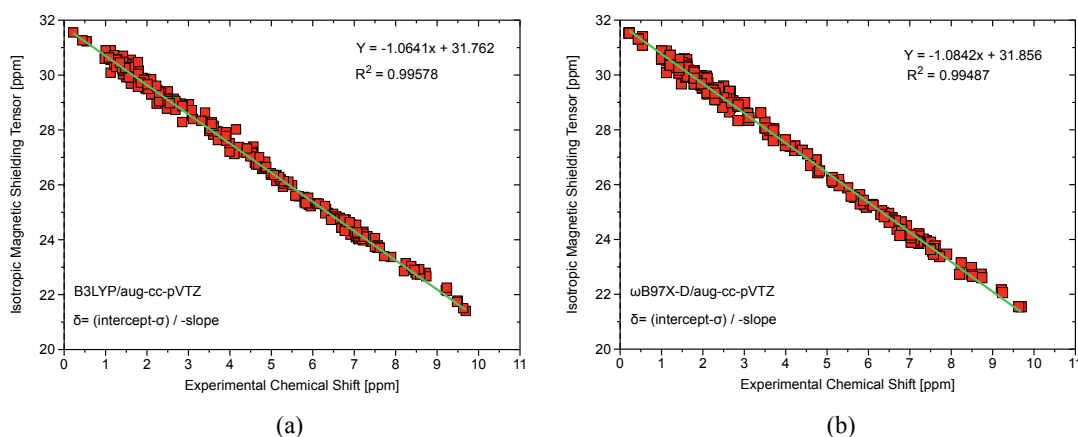
Figure A1. (**a**) Computed at the B3LYP/aug-cc-pVTZ level of theory, isotropic magnetic shielding tensors plotted against experimental NMR chemical shifts showing strong linear correlation and a slope close to −1 which is indicative of minimization of systematic error. (**b**) Computed at the ωB97X-D/aug-cc-pVTZ level of theory, isotropic magnetic shielding tensors plotted against experimental NMR chemical shifts again showing strong linear correlation and slope close to −1.

References

1. Kieltsch, I.; Eisenberger, P.; Togni, A. Mild Electrophilic Trifluoromethylation of Carbon- and Sulfur-Centered Nucleophiles by a Hypervalent Iodine(III)–CF$_3$ Reagent. *Angew. Chem. Int.* **2007**, *46*, 754–757. [CrossRef] [PubMed]
2. Silva, F.C.S.; Tierno, A.F.; Wengryniuk, S.E. Hypervalent Iodine Reagents in High Valent Transition Metal Chemistry. *Molecules* **2017**, *22*, 780. [CrossRef]
3. Charpentier, J.; Früh, N.; Togni, A. Electrophilic Trifluoromethylation by Use of Hypervalent Iodine Reagents. *Chem. Rev.* **2014**, *115*, 650–682. [CrossRef] [PubMed]
4. Maddox, V.H.; Godefroi, E.F.; Parcell, R.F. The Synthesis of Phencyclidine and Other 1-Arylcyclohexylamines. *J. Med. Chem.* **1965**, *8*, 230–235. [CrossRef] [PubMed]
5. Moriarty, R.M.; Enache, L.A.; Zhao, L.; Gilardi, R.; Mattson, M.V.; Prakash, O. Rigid Phencyclidine Analogues. Binding to the Phencyclidine and σ1 Receptors. *J.Med. Chem.* **1998**, *41*, 468–477. [CrossRef]

6.　Berger, G.; Soubhye, J.; Meyer, F. Halogen bonding in polymer science: From crystal engineering to functional supramolecular polymers and materials. *Polym. Chem.* **2015**, *6*, 3559–3580. [CrossRef]

7.　Murphy, G.K.; Racicot, L.; Carle, M.S. The Chemistry between Hypervalent Iodine(III) Reagents and Organophosphorus Compounds. *Asian J. Org. Chem.* **2018**, *7*, 837–851. [CrossRef]

8.　Ghosh, S.; Pradhan, S.; Chatterjee, I. A survey of chiral hypervalent iodine reagents in asymmetric synthesis. *Beilstein J. Org. Chem* **2018**, *14*, 1244–1262. [CrossRef]

9.　Cavallo, G.; Metrangolo, P.; Milani, R.; Pilati, T.; Priimagi, A.; Resnati, G.; Terraneo, G. The Halogen Bond. *Chem. Rev.* **2016**, *116*, 2478–2601. [CrossRef] [PubMed]

10.　Wulfsberg, G. *Inorganic Chemistry*; University Science Books: Sausalito, CA, USA, 2000.

11.　Crabtree, R.H. Hypervalency, secondary bonding and hydrogen bonding: Siblings under the skin. *Chem. Soc. Rev.* **2017**, *46*, 1720–1729. [CrossRef]

12.　Berger, G.; Soubhye, J.; van der Lee, A.; Vande Velde, C.; Wintjens, R.; Dubois, P.; Clément, S.; Meyer, F. Interplay between Halogen Bonding and Lone Pair-π Interactions: A Computational and Crystal Packing Study. *ChemPlusChem* **2014**, *79*, 552–558. [CrossRef]

13.　Labattut, A.; Tremblay, P.L.; Moutounet, O.; Legault, C.Y. Experimental and Theoretical Quantification of the Lewis Acidity of Iodine(III) Species. *J. Org. Chem.* **2017**, *82*, 11891–11896. [CrossRef] [PubMed]

14.　Kalescky, R.; Zou, W.; Kraka, E.; Cremer, D. Quantitative Assessment of the Multiplicity of Carbon-Halogen Bonds: Carbenium and Halonium Ions with F, Cl, Br, and I. *J. Phys. Chem. A* **2014**, *118*, 1948–1963. [CrossRef] [PubMed]

15.　Kalescky, R.; Kraka, E.; Cremer, D. Are carbon–halogen double and triple bonds possible? *Int. J. Quant. Chem.* **2014**, *114*, 1060–1072. [CrossRef]

16.　Yoshimura, A.; Zhdankin, V.V. Advances in Synthetic Applications of Hypervalent Iodine Compounds. *Chem. Rev.* **2016**, *116*, 3328–3435. [CrossRef] [PubMed]

17.　Zhdankin, V.V.; Stang, P.J. Chemistry of Polyvalent Iodine. *Chem. Rev.* **2008**, *108*, 5299–5358. [CrossRef] [PubMed]

18.　Archer, E.M.; van Schalkwyk, T.G. The crystal structure of benzene iododichloride. *Acta. Crystallogr. A* **1953**, *6*, 88–92. [CrossRef]

19.　Landrum, G.A.; Goldberg, N.; Hoffmann, R.; Minyaev, R.M. Intermolecular interactions between hypervalent molecules: Ph_2IX and XF_3 (X = Cl, Br, I) dimers. *New J. Chem.* **1998**, *22*, 883–890. [CrossRef]

20.　Bersuker, I.B. Modern Aspects of the Jahn–Teller Effect Theory and Applications To Molecular Problems. *Chem. Rev.* **2001**, *101*, 1067–1114. [CrossRef]

21.　Batsanov, S.S. Van der Waals Radii of Elements. *Inorg. Mater.* **2001**, *37*, 871–885. [CrossRef]

22.　Nyburg, S.C.; Faerman, C.H.; Prasad, L. A revision of van der Waals atomic radii for molecular crystals. II: Hydrogen bonded to carbon. *Acta Crystallogr. B* **1987**, *43*, 106–110. [CrossRef]

23.　Nyburg, S.C.; Faerman, C.H. A revision of van der Waals atomic radii for molecular crystals: N, O, F, S, Cl, Se, Br and I bonded to carbon. *Acta Crystallogr. B* **1985**, *41*, 274–279. [CrossRef]

24.　Ishikawa, M.; Ikuta, S.; Katada, M.; Sano, H. Anisotropy of van der Waals radii of atoms in molecules: Alkali-metal and halogen atoms. *Acta Crystallogr. B* **1990**, *46*, 592–598. [CrossRef]

25.　Badenhoop, J.K.; Weinhold, F. Natural steric analysis: Ab initio van der Waals radii of atoms and ions. *J. Chem. Phys.* **1997**, *107*, 5422–5432. [CrossRef]

26.　Bader, R.F.W.; Henneker, W.H.; Cade, P.E. Molecular Charge Distributions and Chemical Binding. *J. Chem. Phys.* **1967**, *46*, 3341–3363. [CrossRef]

27.　Bader, R.F.W.; Carroll, M.T.; Cheeseman, J.R.; Chang, C. Properties of atoms in molecules: Atomic volumes. *J. Am. Chem. Soc.* **1987**, *109*, 7968–7979. [CrossRef]

28.　Bader, R.F.W.; Bandrauk, A.D. Relaxation of the Molecular Charge Distribution and the Vibrational Force Constant. *J. Chem. Phys.* **1968**, *49*, 1666–1675. [CrossRef]

29.　Molina, J.M.; Dobado, J.A. The three-center-four-electron (3c–4e) bond nature revisited. An atoms-in-molecules theory (AIM) and ELF study. *Theor. Chim. Acta.* **2001**, *105*, 328–337. [CrossRef]

30.　Musher, J.I. The Chemistry of Hypervalent Molecules. *Angew. Chem. Ed.* **1969**, *8*, 54–68. [CrossRef]

31.　Reed, A.E.; von Ragué Schleyer, P. Chemical Bonding in Hypervalent Molecules. The Dominance of Ionic Bonding and Negative Hyperconjugation over d-orbital Participation. *J. Am. Chem. Soc.* **1990**, *112*, 1434–1445. [CrossRef]

32. Magnusson, E. Hypercoordinate Molecules of Second-Row Elements: d Functions or d Orbitals? *J. Am. Chem. Soc.* **1990**, *112*, 7940–7951. [CrossRef]

33. Landrum, G.A.; Goldberg, N.; Hoffmann, R. Bonding in the trihalides (X^{3-}), mixed trihalides (X_2Y^-) and hydrogen bihalides (X_2H^-). The connection between hypervalent, electron-rich three-center, donor-acceptor and strong hydrogen bonding. *Dalton Trans.* **1997**, *0*, 3605–3613. [CrossRef]

34. Yang, L.M.; Ganz, E.; Chen, Z.; Wang, Z.X.; von Ragué Schleyer, P. Four Decades of the Chemistry of Planar Hypercoordinate Compounds. *Angew. Chem. Int. Ed.* **2015**, *54*, 9468–9501. [CrossRef]

35. Oliveira, V.; Kraka, E.; Cremer, D. The intrinsic strength of the halogen bond: Electrostatic and covalent contributions described by coupled cluster theory. *Phys. Chem. Chem. Phys.* **2016**, *18*, 33031–33046. [CrossRef]

36. Wolters, L.P.; Bickelhaupt, F.M. Halogen Bonding versus Hydrogen Bonding: A Molecular Orbital Perspective. *ChemistryOpen* **2012**, *1*, 96–105. [CrossRef]

37. Cozzolino, A.F.; Elder, P.J.; Vargas-Baca, I. A survey of tellurium-centered secondary-bonding supramolecular synthons. *Coord. Chem. Rev.* **2011**, *255*, 1426–1438. [CrossRef]

38. Freindorf, M.; Kraka, E.; Cremer, D. A comprehensive analysis of hydrogen bond interactions based on local vibrational modes. *Int. J. Quant. Chem.* **2012**, *112*, 3174–3187. [CrossRef]

39. Scheiner, S. Detailed comparison of the pnicogen bond with chalcogen, halogen, and hydrogen bonds. *Int. J. Quantum Chem.* **2012**, *113*, 1609–1620. [CrossRef]

40. Scheiner, S. The Pnicogen Bond: Its Relation to Hydrogen, Halogen, and Other Noncovalent Bonds. *Acc. Chem. Res.* **2012**, *46*, 280–288. [CrossRef] [PubMed]

41. Oliveira, V.; Kraka, E.; Cremer, D. Quantitative Assessment of Halogen Bonding Utilizing Vibrational Spectroscopy. *Inorg. Chem.* **2016**, *56*, 488–502. [CrossRef] [PubMed]

42. Oliveira, V.; Cremer, D. Transition from metal–ligand bonding to halogen bonding involving a metal as halogen acceptor a study of Cu, Ag, Au, Pt, and Hg complexes. *Chem. Phys. Lett.* **2017**, *681*, 56–63. [CrossRef]

43. Oliveira, V.; Kraka, E. Systematic Coupled Cluster Study of Noncovalent Interactions Involving Halogens, Chalcogens, and Pnicogens. *J. Phys. Chem. A* **2017**, *121*, 9544–9556. [CrossRef] [PubMed]

44. Setiawan, D.; Kraka, E.; Cremer, D. Description of pnicogen bonding with the help of vibrational spectroscopy—The missing link between theory and experiment. *Chem. Phys. Lett.* **2014**, *614*, 136–142. [CrossRef]

45. Setiawan, D.; Kraka, E.; Cremer, D. Strength of the Pnicogen Bond in Complexes Involving Group VA Elements N, P, and As. *J. Phys. Chem. A* **2014**, *119*, 1642–1656. [CrossRef] [PubMed]

46. Tao, Y.; Tian, C.; Verma, N.; Zou, W.; Wang, C.; Cremer, D.; Kraka, E. Recovering Intrinsic Fragmental Vibrations Using the Generalized Subsystem Vibrational Analysis. *J. Chem. Theory Comput.* **2018**, *14*, 2558–2569. [CrossRef] [PubMed]

47. Kraka, E.; Cremer, D. Dieter Cremer's Contribution to the Field of Theoretical Chemistry. *Int. J. Quantum Chem.* **2019**, *119*, e25849. [CrossRef]

48. Bene, J.D.; Alkorta, I.; Elguero, J. Halogen Bonding Involving CO and CS with Carbon as the Electron Donor. *Molecules* **2017**, *22*, 1955. [CrossRef]

49. Alkorta, I.; Elguero, J.; Bene, J.E.D. Boron as an Electron-Pair Donor for B···Cl Halogen Bonds. *ChemPhysChem.* **2016**, *17*, 3112–3119. [CrossRef]

50. Oliveira, V.; Cremer, D.; Kraka, E. The Many Facets of Chalcogen Bonding: Described by Vibrational Spectroscopy. *J. Phys. Chem. A* **2017**, *121*, 6845–6862. [CrossRef]

51. Bene, J.E.D.; Alkorta, I.; Elguero, J. Hydrogen and Halogen Bonding in Cyclic $FH_{(4-n)}$:FCl_n Complexes, for $n = 0–4$. *J. Phys. Chem. A* **2018**, *122*, 2587–2597. [CrossRef] [PubMed]

52. Cavallo, G.; Murray, J.S.; Politzer, P.; Pilati, T.; Ursini, M.; Resnati, G. Halogen bonding in hypervalent iodine and bromine derivatives: Halonium salts. *IUCrJ* **2017**, *4*, 411–419. [CrossRef]

53. Heinen, F.; Engelage, E.; Dreger, A.; Weiss, R.; Huber, S.M. Iodine(III) Derivatives as Halogen Bonding Organocatalysts. *Angew. Chem. Int. Ed.* **2018**, *57*, 3830–3833. [CrossRef] [PubMed]

54. Zhdankin, V.V. *Hypervalent Iodine Chemistry: Preparation, Structure, and Synthetic Applications of Polyvalent Iodine Compounds*; John Wiley and Sons Ltd.: West Sussex, UK, 2014.

55. Cremer, D.; Kraka, E. A Description of the Chemical Bond in Terms of Local Properties of Electron Density and Energy. *Croatica Chem. Acta* **1984**, *57*, 1259–1281.

56. Cremer, D. New Ways of Analyzing Chemical Bonding. In *Modelling of Structure and Properties of Molecules*; Maksic, Z.B., Ed.; Ellis Horwood: Chichester, UK, 1987; p. 125.

57. Kraka, E.; Cremer, D. Chemical Implication of Local Features of the Electron Density Distribution. In *Theoretical Models of Chemical Bonding. The Concept of the Chemical Bond*; Maksic, Z.B., Ed.; Springer: Heidelberg, Germany, 1990; Volume 2, p. 453.

58. Wang, C.; Danovich, D.; Mo, Y.; Shaik, S. On The Nature of the Halogen Bond. *J. Chem. Theory Comput.* **2014**, *10*, 3726–3737. [CrossRef]

59. Wang, C.; Guan, L.; Danovich, D.; Shaik, S.; Mo, Y. The origins of the directionality of noncovalent intermolecular interactions. *J. Comput. Chem.* **2015**, *37*, 34–45. [CrossRef] [PubMed]

60. Konkoli, Z.; Cremer, D. A new way of analyzing vibrational spectra. I. Derivation of adiabatic internal modes. *Int. J. Quant. Chem.* **1998**, *67*, 1–9. [CrossRef]

61. Konkoli, Z.; Larsson, J.A.; Cremer, D. A new way of analyzing vibrational spectra. IV. Application and testing of adiabatic modes within the concept of the characterization of normal modes. *Int. J. Quant. Chem.* **1998**, *67*, 41–55. [CrossRef]

62. Cremer, D.; Larsson, J.A.; Kraka, E. New developments in the analysis of vibrational spectra On the use of adiabatic internal vibrational modes. In *Theoretical and Computational Chemistry*; Parkanyi, C., Ed.; Elsevier: Amsterdam, The Netherlands, 1998; pp. 259–327.

63. Alcock, N.W.; Countryman, R.M. Secondary bonding. Part 4. The crystal and molecular structure of μ-oxo-bis[nitrato(phenyl)iodine(III)]. *J. Chem. Soc., Dalton Trans.* **1979**, *0*, 851–853. [CrossRef]

64. Hoyer, S.; Seppelt, K. The structure of IF3. *Angew. Chem. Int. Ed.* **2000**, *39*, 1448–1449. [CrossRef]

65. Boldyrev, A.I.; Zhdankin, V.V.; Simons, J.; Stang, P.J. Macrocyclic, square planar, tetraalkynyl tetraiodonium salts: Structures, stabilities, and vibrational frequencies via ab initio calculations. *J. Am. Chem. Soc.* **1992**, *114*, 10569–10572. [CrossRef]

66. Boswijk, K.H.; Wiebenga, E.H. The crystal structure of I_2Cl_6 (ICl_3). *Acta Crystallogr.* **1954**, *7*, 417–423. [CrossRef]

67. Grimme, S. Semiempirical hybrid density functional with perturbative second-order correlation. *J. Chem. Phys.* **2006**, *124*, 034108. [CrossRef] [PubMed]

68. Woon, D.E.; Dunning, T.H. Gaussian basis sets for use in correlated molecular calculations. III. The atoms aluminum through argon. *J. Chem. Phys.* **1993**, *98*, 1358–1371. [CrossRef]

69. Dunning, T.H. Gaussian basis sets for use in correlated molecular calculations. I. The atoms boron through neon and hydrogen. *J. Chem. Phys.* **1989**, *90*, 1007–1023. [CrossRef]

70. Kendall, R.A.; Dunning, T.H.; Harrison, R.J. Electron affinities of the first? Row atoms revisited. Systematic basis sets and wave functions. *J. Chem. Phys.* **1992**, *96*, 6796–6806. [CrossRef]

71. Woon, D.E.; Dunning, T.H. Gaussian basis sets for use in correlated molecular calculations. IV. Calculation of static electrical response properties. *J. Chem. Phys.* **1994**, *100*, 2975–2988. [CrossRef]

72. Becke, A.D. Density-functional thermochemistry. III. The role of exact exchange. *J. Chem. Phys.* **1993**, *98*, 5648–5652. [CrossRef]

73. Becke, A.D. Density-functional thermochemistry. V. Systematic optimization of exchange-correlation functionals. *J. Chem. Phys.* **1997**, *107*, 8554–8560. [CrossRef]

74. Lee, C.; Yang, W.; Parr, R.G. Development of the Colle-Salvetti correlation-energy formula into a functional of the electron density. *Phys. Rev. B* **1988**, *37*, 785–789. [CrossRef]

75. Møller, C.; Plesset, M.S. Note on an Approximation Treatment for Many-Electron Systems. *Phys. Rev.* **1934**, *46*, 618–622. [CrossRef]

76. Head-Gordon, M.; Pople, J.A.; Frisch, M.J. MP2 energy evaluation by direct methods. *Chem. Phys. Lett.* **1988**, *153*, 503–506. [CrossRef]

77. Cremer, D. Møller-Plesset Perturbation Theory. In *Encyclopedia of Computational Chemistry*; Schleyer, P., Allinger, N., Clark, T., Gasteiger, J., Kollman, P., Schaefer, H., III, Schreiner, P., Eds.; John Wiley & Sons: New York, NY, USA, 1998; pp. 1706–1735.

78. Cremer, D. Møller-Plesset perturbation theory: From small molecule methods to methods for thousands of atoms. *WIREs Comput. Mol. Sci.* **2011**, *1*, 509–530. [CrossRef]

79. Görling, A.; Levy, M. Correlation-energy functional and its high-density limit obtained from a coupling-constant perturbation expansion. *Phys. Rev. B* **1993**, *47*, 13105–13113. [CrossRef]

80. Görling, A.; Levy, M. Exact Kohn-Sham scheme based on perturbation theory. *Phys. Rev. A* **1994**, *50*, 196–204. [CrossRef] [PubMed]

81. Mori-Sánchez, P.; Wu, Q.; Yang, W. Orbital-dependent correlation energy in density-functional theory based on a second-order perturbation approach: Success and failure. *J. Chem. Phys.* **2005**, *123*, 062204. [CrossRef] [PubMed]

82. Biczysko, M.; Panek, P.; Scalmani, G.; Bloino, J.; Barone, V. Harmonic and Anharmonic Vibrational Frequency Calculations with the Double-Hybrid B2PLYP Method: Analytic Second Derivatives and Benchmark Studies. *J. Chem. Theory Comput.* **2010**, *6*, 2115–2125. [CrossRef] [PubMed]

83. Bousquet, D.; Brémond, E.; Sancho-García, J.C.; Ciofini, I.; Adamo, C. Is There Still Room for Parameter Free Double Hybrids? Performances of PBE0-DH and B2PLYP over Extended Benchmark Sets. *J. Chem. Theory Comput.* **2013**, *9*, 3444–3452. [CrossRef]

84. Sinnokrot, M.O.; Sherrill, C.D. High-Accuracy Quantum Mechanical Studies of $\pi-\pi$ Interactions in Benzene Dimers. *J. Phys. Chem. A* **2006**, *110*, 10656–10668. [CrossRef] [PubMed]

85. Shibasaki, K.; Fujii, A.; Mikami, N.; Tsuzuki, S. Magnitude of the CH/π Interaction in the Gas Phase: Experimental and Theoretical Determination of the Accurate Interaction Energy in Benzene-methane. *J. Phys. Chem. A* **2006**, *110*, 4397–4404. [CrossRef]

86. Janowski, T.; Pulay, P. High accuracy benchmark calculations on the benzene dimer potential energy surface. *Chem. Phys. Lett.* **2007**, *447*, 27–32. [CrossRef]

87. Chai, J.D.; Head-Gordon, M. Long-range corrected hybrid density functionals with damped atom–atom dispersion corrections. *Phys. Chem. Chem. Phys.* **2008**, *10*, 6615–6620. [CrossRef] [PubMed]

88. Chai, J.D.; Head-Gordon, M. Systematic optimization of long-range corrected hybrid density functionals. *J. Chem. Phys.* **2008**, *128*, 084106. [CrossRef] [PubMed]

89. Peterson, K.A. Systematically convergent basis sets with relativistic pseudopotentials. I. Correlation consistent basis sets for the post-d group 13–15 elements. *J. Chem. Phys.* **2003**, *119*, 11099–11112. [CrossRef]

90. Peterson, K.A.; Figgen, D.; Goll, E.; Stoll, H.; Dolg, M. Systematically convergent basis sets with relativistic pseudopotentials. II. Small-core pseudopotentials and correlation consistent basis sets for the post-d group 16-18 elements. *J. Chem. Phys.* **2003**, *119*, 11113–11123. [CrossRef]

91. London, F. The quantic theory of inter-atomic currents in aromatic combinations. *J. Phys. Radium* **1937**, *8*, 397–409. [CrossRef]

92. McWeeny, R. Perturbation Theory for the Fock-Dirac Density Matrix. *Phys. Rev.* **1962**, *126*, 1028–1034. [CrossRef]

93. Ditchfield, R. Self-consistent perturbation theory of diamagnetism. 1. Gauge-invariant LCAO method for N.M.R. chemical shifts. *Mol. Phys.* **1974**, *27*, 789–807. [CrossRef]

94. Wolinski, K.; Hinton, J.F.; Pulay, P. Efficient implementation of the gauge-independent atomic orbital method for NMR chemical shift calculations. *J. Am. Chem. Soc.* **1990**, *112*, 8251–8260. [CrossRef]

95. Cheeseman, J.R.; Trucks, G.W.; Keith, T.A.; Frisch, M.J. A comparison of models for calculating nuclear magnetic resonance shielding tensors. *J. Chem. Phys.* **1996**, *104*, 5497–5509. [CrossRef]

96. Rablen, P.R.; Pearlman, S.A.; Finkbiner, J. A Comparison of Density Functional Methods for the Estimation of Proton Chemical Shifts with Chemical Accuracy. *J. Phys. Chem. A* **1999**, *103*, 7357–7363. [CrossRef]

97. Jain, R.; Bally, T.; Rablen, P.R. Calculating Accurate Proton Chemical Shifts of Organic Molecules with Density Functional Methods and Modest Basis Sets. *J. Org. Chem.* **2009**, *74*, 4017–4023. [CrossRef]

98. Bally, T.; Rablen, P.R. Quantum-Chemical Simulation of ^1H NMR Spectra. 2.† Comparison of DFT-Based Procedures for Computing Proton-Proton Coupling Constants in Organic Molecules. *J. Org. Chem.* **2011**, *76*, 4818–4830. [CrossRef] [PubMed]

99. Lodewyk, M.W.; Siebert, M.R.; Tantillo, D.J. Computational Prediction of 1H and 13C Chemical Shifts: A Useful Tool for Natural Product, Mechanistic, and Synthetic Organic Chemistry. *Chem. Rev.* **2011**, *112*, 1839–1862. [CrossRef]

100. Lodewyk, M.W.; Soldi, C.; Jones, P.B.; Olmstead, M.M.; Rita, J.; Shaw, J.T.; Tantillo, D.J. The Correct Structure of Aquatolide-Experimental Validation of a Theoretically-Predicted Structural Revision. *J. Am. Chem. Soc.* **2012**, *134*, 18550–18553. [CrossRef]

101. Lodewyk, M.W.; Tantillo, D.J. Prediction of the Structure of Nobilisitine A Using Computed NMR Chemical Shifts. *J. Nat. Prod.* **2011**, *74*, 1339–1343. [CrossRef]

102. Brand, J.; Charpentier, J.; Waser, J. Direct Alkynylation of Indole and Pyrrole Heterocycles. *Angew. Chem. Int. Ed.* **2009**, *48*, 9346–9349. [CrossRef] [PubMed]

103. Cremer, D.; Kraka, E. From Molecular Vibrations to Bonding, Chemical Reactions, and Reaction Mechanism. *Curr. Org. Chem.* **2010**, *14*, 1524–1560. [CrossRef]

104. Kraka, E.; Larsson, J.A.; Cremer, D. Generalization of the Badger Rule Based on the Use of Adiabatic Vibrational Modes. In *Computational Spectroscopy*; Grunenberg, J., Ed.; Wiley: New York, NY, USA, 2010; pp. 105–149.

105. Wilson, E.B.; Decius, J.C.; Cross, P.C. *Molecular Vibrations: The Theory of Infrared and Raman Vibrational Spectra*; McGraw-Hill: New York, NY, USA, 1955.

106. Konkoli, Z.; Larsson, J.A.; Cremer, D. A new way of analyzing vibrational spectra. II. Comparison of internal mode frequencies. *Int. J. Quant. Chem.* **1998**, *67*, 11–27. [CrossRef]

107. Zou, W.; Kalescky, R.; Kraka, E.; Cremer, D. Relating Normal Vibrational Modes to Local Vibrational Modes with the Help of an Adiabatic Connection Scheme. *J. Chem. Phys.* **2012**, *137*, 084114. [CrossRef]

108. Kalescky, R.; Zou, W.; Kraka, E.; Cremer, D. Local vibrational modes of the water dimer — Comparison of theory and experiment. *Chem. Phys. Lett.* **2012**, *554*, 243–247. [CrossRef]

109. Zou, W.; Kalescky, R.; Kraka, E.; Cremer, D. Relating normal vibrational modes to local vibrational modes: benzene and naphthalene. *J. Mol. Model.* **2012**, *19*, 2865–2877. [CrossRef]

110. Kalescky, R.; Kraka, E.; Cremer, D. Local vibrational modes of the formic acid dimer—The strength of the double hydrogen bond. *Mol. Phys.* **2013**, *111*, 1497–1510. [CrossRef]

111. Kalescky, R.; Kraka, E.; Cremer, D. New Approach to Tolman's Electronic Parameter Based on Local Vibrational Modes. *Inorg. Chem.* **2013**, *53*, 478–495. [CrossRef]

112. Konkoli, Z.; Cremer, D. A new way of analyzing vibrational spectra. III. Characterization of normal vibrational modes in terms of internal vibrational modes. *Int. J. Quant. Chem.* **1998**, *67*, 29–40. [CrossRef]

113. Zou, W.; Cremer, D. C_2 in a Box: Determining its Intrinsic Bond Strength for the $X^1 \Sigma^+_g$ Ground State. *Chem. Eur. J.* **2016**, *22*, 4087–4097. [CrossRef] [PubMed]

114. Setiawan, D.; Kraka, E.; Cremer, D. Hidden Bond Anomalies: The Peculiar Case of the Fluorinated Amine Chalcogenides. *J. Phys. Chem. A* **2015**, *119*, 9541–9556. [CrossRef] [PubMed]

115. Kraka, E.; Setiawan, D.; Cremer, D. Re-evaluation of the bond length-bond strength rule: The stronger bond is not always the shorter bond. *J. Comp. Chem.* **2015**, *37*, 130–142. [CrossRef] [PubMed]

116. Setiawan, D.; Sethio, D.; Cremer, D.; Kraka, E. From Strong to Weak NF Bonds: On the Design of a New Class of Fluorinating Agents. *Phys. Chem. Chem. Phys.* **2018**, *20*, 23913–23927. [CrossRef] [PubMed]

117. Tao, Y.; Zou, W.; Jia, J.; Li, W.; Cremer, D. Different Ways of Hydrogen Bonding in Water—Why Does Warm Water Freeze Faster than Cold Water? *J. Chem. Theory Comput.* **2016**, *13*, 55–76. [CrossRef]

118. Tao, Y.; Zou, W.; Kraka, E. Strengthening of hydrogen bonding with the push-pull effect. *Chem. Phys. Lett.* **2017**, *685*, 251–258. [CrossRef]

119. Li, Y.; Oliveira, V.; Tang, C.; Cremer, D.; Liu, C.; Ma, J. The Peculiar Role of the Au_3 Unit in Au_m Clusters: σ-Aromaticity of the Au_5Zn^+ Ion. *Inorg. Chem.* **2017**, *56*, 5793–5803. [CrossRef] [PubMed]

120. Zhang, X.; Dai, H.; Yan, H.; Zou, W.; Cremer, D. B–H π Interaction: A New Type of Nonclassical Hydrogen Bonding. *J. Am. Chem. Soc.* **2016**, *138*, 4334–4337. [CrossRef] [PubMed]

121. Zou, W.; Zhang, X.; Dai, H.; Yan, H.; Cremer, D.; Kraka, E. Description of an unusual hydrogen bond between carborane and a phenyl group. *J. Organometal. Chem.* **2018**, *865*, 114–127. [CrossRef]

122. Setiawan, D.; Kalescky, R.; Kraka, E.; Cremer, D. Direct Measure of Metal–Ligand Bonding Replacing the Tolman Electronic Parameter. *Inorg. Chem.* **2016**, *55*, 2332–2344. [CrossRef]

123. Cremer, D.; Kraka, E. Generalization of the Tolman electronic parameter: The metal–ligand electronic parameter and the intrinsic strength of the metal–ligand bond. *Dalton Trans.* **2017**, *46*, 8323–8338. [CrossRef]

124. Setiawan, D.; Kraka, E.; Cremer, D. Quantitative Assessment of Aromaticity and Antiaromaticity Utilizing Vibrational Spectroscopy. *J. Org. Chem.* **2016**, *81*, 9669–9686. [CrossRef] [PubMed]

125. Badger, R.M. A Relation Between Internuclear Distances and Bond Force Constants. *J. Chem. Phys.* **1934**, *2*, 128–131. [CrossRef]

126. Mayer, I. Bond order and valence indices: A personal account. *J. Comput. Chem.* **2006**, *28*, 204–221. [CrossRef]

127. Cremer, D.; Kraka, E. Chemical Bonds without Bonding Electron Density? Does the Difference Electron-Density Analysis Suffice for a Description of the Chemical Bond? *Angew. Chem. Int. Ed.* **1984**, *23*, 627–628. [CrossRef]

128. Sánchez-Sanz, G.; Trujillo, C.; Alkorta, I.; Elguero, J. Electron density shift description of non-bonding intramolecular interactions. *Comput. Theor. Chem.* **2012**, *991*, 124–133. [CrossRef]

129. Kraka, E.; Zou, W.; Filatov, M.; Tao, Y.; Grafenstein, J.; Izotov, D.; Gauss, J.; He, Y.; Wu, A.; Konkoli, Z.; et al. COLOGNE2018. 2018. Available online: http://www.smu.edu/catco (accessed on 15 April 2018).

130. Neese, F. The ORCA program system. *Wiley Interdiscip. Rev. Comput. Mol. Sci.* **2011**, *2*, 73–78. [CrossRef]

131. Reed, A.E.; Curtiss, L.A.; Weinhold, F. Intermolecular interactions from a natural bond orbital, donor-acceptor viewpoint. *Chem. Rev.* **1988**, *88*, 899–926. [CrossRef]

132. Sosa, G.L.; Peruchena, N.M.; Contreras, R.H.; Castro, E.A. Topological and NBO analysis of hydrogen bonding interactions involving C–H···O bonds. *J. Mol. Struct. THEOCHEM* **2002**, *577*, 219–228. [CrossRef]

133. Reed, A.E.; Weinstock, R.B.; Weinhold, F. Natural population analysis. *J. Chem. Phys.* **1985**, *83*, 735–746. [CrossRef]

134. Reed, A.E.; Weinhold, F. Natural localized molecular orbitals. *J. Chem. Phys.* **1985**, *83*, 1736–1740. [CrossRef]

135. Bader, R.F.W. A quantum theory of molecular structure and its applications. *Chem. Rev.* **1991**, *91*, 893–928. [CrossRef]

136. Keith, T.A. AIMAll (Version 17.11.14). 2017. Available online: aim.tkgristmill.com (accessed on 2 April 2018).

137. Frisch, M.J.; Trucks, G.W.; Schlegel, H.B.; Scuseria, G.E.; Robb, M.A.; Cheeseman, J.R.; Scalmani, G.; Barone, V.; Petersson, G.A.; Nakatsuji, H.; et al. *Gaussian16 Revision B.01*; Gaussian Inc.: Wallingford, CT, USA, 2016.

138. Clark, T.; Murray, J.S.; Politzer, P. The σ-Hole Coulombic Interpretation of Trihalide Anion Formation. *ChemPhysChem* **2018**, *19*, 3044–3049. [CrossRef]

139. de Magalhães, H.P.; Lüthi, H.P.; Bultinck, P. Exploring the role of the 3-center-4-electron bond in hypervalent λ^3-iodanes using the methodology of domain averaged Fermi holes. *Phys. Chem. Chem. Phys.* **2016**, *18*, 846–856. [CrossRef]

140. Ruedenberg, K. The Physical Nature of the Chemical Bond. *Rev. Mod. Phys.* **1962**, *34*, 326–376. [CrossRef]

141. Bacskay, G.B.; Nordholm, S.; Ruedenberg, K. The Virial Theorem and Covalent Bonding. *J. Phys. Chem. A* **2018**, *122*, 7880–7893. [CrossRef] [PubMed]

142. Zou, W.; Sexton, T.; Kraka, E.; Freindorf, M.; Cremer, D. A New Method for Describing the Mechanism of a Chemical Reaction Based on the Unified Reaction Valley Approach. *J. Chem. Theory Comput.* **2016**, *12*, 650–663. [CrossRef] [PubMed]

143. Kraka, E. Reaction path Hamiltonian and the unified reaction valley approach. *WIREs: Comput. Mol. Sci.* **2011**, *1*, 531–556. [CrossRef]

144. Kraka, E.; Cremer, D. Computational Analysis of the Mechanism of Chemical Reactions in Terms of Reaction Phases: Hidden Intermediates and Hidden Transition States. *Acc. Chem. Res.* **2010**, *43*, 591–601. [CrossRef] [PubMed]

145. Kumar, R.; Vaish, A.; Runčevski, T.; Tsarevsky, N.V. Hypervalent Iodine Compounds with Tetrazole Ligands. *J. Org. Chem.* **2018**, *83*, 12496–12506. [CrossRef]

146. Vaish, A.; Tsarevsky, N. Hypervalent Iodine Compounds in Polymer Science and Technology. In *Main Group Strategies towards Functional Hybrid Materials*; Baumgartner, T., Jaekle, F., Eds.; Wiley: New York, NY, USA, 2018; Chapter 19, pp. 483–514.